Large-eddy simulation of radiation fog: Part 1: Impact of dynamics on microphysics

Marie Mazoyer[1], Christine Lac[1], Odile Thouron[2], Thierry Bergot[1], Valery Masson[1], and Luc Musson-Genon[3]

[1]CNRM (CNRS-Meteo-France), UMR3589, Toulouse, France
[2]CERFACS, Toulouse, France
[3]CEREA, France

Correspondence to: Christine Lac (christine.lac@meteo.fr)

Abstract.

Large Eddy simulations (LES) of a radiation fog event occurring during the ParisFog experiment are studied with a view to analysing the impact of the dynamics of the boundary layer on the microphysics. The LES, performed with the Meso-NH model at 5 m resolution horizontally and 1 m vertically, and with a 2-moment microphysical scheme, includes the drag effect of a tree barrier and the deposition of droplets on vegetation. The model shows good agreement with measurements of near surface dynamic and thermodynamic parameters, but overestimates the cloud droplet mass and concentration. The blocking effect of the trees induces elevated fog formation, as actually observed, and horizontal heterogeneities during the formation. It also limits cooling and cloud water production. Deposition is found to exert the most significant impact on fog prediction as it not only erodes the fog near the surface but also modifies the fog life cycle and induces vertical heterogeneities. A comparison with the 2 m horizontal resolution simulation reveals small differences, meaning that grid convergence is achieved. Conversely, increasing numerical diffusion through a wind advection operator of lower order leads to an overestimation of the near-surface microphysical fields and has a very similar effect to removing the tree barrier. This study allows us to establish the major dynamical ingredients needed to accurately represent the fog life cycle at very high resolution.

1 Introduction

Despite long-standing interest in understanding fog processes, uncertainties still exist in the physical mechanisms driving fog variability. Forecasting fog remains a challenge because of the diversity of mechanisms involved during the fog life cycle and their interactions: local flow, turbulence, radiation, microphysics, aerosols, and surface effects. Several field experiments have been carried out since the 1970s and have contributed to the important progress made in understanding fog processes. Noteworthy studies include campaigns at Cardington in the UK (Roach et al., 1976; Price, 2011), Fog-82 in Albany, New York (Meyer et al., 1986), Lille 91 in France (Guedalia and Bergot, 1994), a campaign in the Po Valley in Italy (Fuzzi et al., 1998) and ParisFog in France (Haeffelin et al., 2010). Most of these have included measurements of fog droplet spectra and have reported liquid water contents (LWC) in the range of $0.01 - 0.4\ \mathrm{g\,m^{-3}}$ and droplet number concentrations (N_c) of a few tens to a hundred per $\mathrm{cm^3}$. Roach et al. (1976) reported values of LWC between 0.05 and $0.22\ \mathrm{g\,m^{-3}}$ and N_c between 30 and

$100\ \mathrm{cm}^{-3}$ for winter fog cases at Cardington. More recently, Mazoyer et al. (2016) reported N_c of less than $150\ \mathrm{cm}^{-3}$ for radiation fog over 3 winters during ParisFog.

Many important features of fog have also been characterized using one-dimensional (1D) modelling (Bergot et al., 2007; Tardif, 2007; Stolaki et al., 2015). However, to study some aspects of the characteristics of a fog layer, it has become necessary to explicitly simulate turbulence motions in 3D as shown by Nakanishi (2000), who was the first to use a large-eddy simulation (LES) for fog. LES is a turbulence modelling technique in which most of the energy-containing eddies are explicitly resolved while eddies smaller than a certain cutoff size, usually taken equal to the grid spacing, are parametrized by a turbulence scheme. Since then, Porson et al. (2011) have explored the static stability in a fog layer, and Bergot (2013) has shown the various organized structures occurring in a fog layer, which cannot be resolved in 1D. Thanks to these studies, the dynamical characteristics of radiation fog are more clearly identified during the three stages of the fog life cycle defined by Nakanishi (2000): the onset, development and dissipation phases. During the formation phase, small banded structures, identified by Bergot (2013) as Kelvin-Helmholtz (KH) billows, occur in the middle of the fog layer in dynamical and thermodynamical fields. They are sometimes associated with a burst of turbulent kinetic energy (TKE) (Nakanishi, 2000; Bergot, 2013) but this is not always the case (Porson et al., 2011). During the development phase, the main dynamical processes relocate to the top of the fog layer and are associated with the maximum of TKE and horizontal rolls (Bergot, 2013). During the dissipation phase, coupled processes between the ground and the top of the fog layer explain the spatial variability of fog (Bergot, 2015b) but the link between dynamics and microphysics has not been explored specifically in these LES studies.

The quality of the LES depends on the horizontal and vertical resolutions. Beare and MacVean (2004) demonstrate that simulations in stable conditions converge at 2-m horizontal resolution. Very high vertical resolution is also essential for representing the divergence of the radiative fluxes in the first few metres above the surface and therefore to produce the radiative cooling necessary for the formation of fog (Duynkerke, 1999; Tardif, 2007).

So far, most fog LES studies have considered homogeneous canopies. Only Bergot et al. (2015a) have accounted for the effect of surface heterogeneities such as buildings on radiation fog. Other studies, such as those by Zaïdi et al. (2013) or Dupont and Brunet (2008), have considered the impact of forests on turbulence structures but not for fog situations. In this study, we will explore an LES of a fog case that was observed during ParisFog and was strongly influenced by trees.

Few fog LES studies are based on sophisticated 2-moment microphysical schemes which allow the impact of aerosols on the radiation fog life cycle to be represented. Maalick et al. (2016) studied the effects of aerosols on radiation fog with an LES but in a 2D configuration that could present some limitations for the dynamical patterns of the fog layer. Additionally, most of the studies using one- or two-moment microphysical schemes fail to reproduce realistic liquid water contents as they tend to overestimate values near the ground. For instance, Zhang et al. (2014b) simulated $N_c = 800\ \mathrm{cm}^{-3}$ and $LWC = 0.4\ \mathrm{g\,m}^{-3}$ and Stolaki et al. (2015) simulated $N_c = 250\ \mathrm{cm}^{-3}$ and $LWC = 0.34\ \mathrm{g\,m}^{-3}$ near the surface, both in 1D configuration. These values are outside the range found by Mazoyer et al. (2016) for the same site. So the question of a possible missing mechanism arises, the inclusion of which might improve the modelling of microphysical fields. Some aspect of deposition that relates to the interaction with the ground surface is important as already shown by Price and Clark (2014) on measurements and von Glasow and Bott (1999) or Zhang et al. (2014b) on 1D simulations.

The goal of this study is to better understand the physical processes dominating the fog life cycle at a complex site and impacting the microphysical fields. LES modelling at very high resolution (1 m vertically and 5 m horizontally) is used with surface heterogeneities (barrier of trees) and a 2-moment microphysical scheme. In order to establish the main ingredients driving the fog life cycle and the microphysical fields, and to evaluate how dynamics affects the evolution of fog, sensitivity simulations are conducted. To our knowledge, this is the first time that an LES study of radiation fog has been performed at such high resolution with a sophisticated microphysical parameterization scheme while considering the effect of heterogeneities such as forests on the fog dynamics and microphysics. In a second article, the impact of aerosol activation on microphysical fields will be explored specifically, allowing the contribution of the different microphysical processes to be characterized.

Section 2 presents the measurement set-up and the observed case, and describes the numerical model. The reference simulation is analysed in Section 3, and Section 4 is devoted to sensitivity tests. Finally, some conclusions are drawn and perspectives suggested in Section 5.

2 Experimental design and model description

2.1 Measurements set-up

The selected fog event was observed on 15 November 2011 during the ParisFog field campaign (Haeffelin et al., 2010) at the Sirta (Site Instrumental de Recherche par Télédétection Atmosphérique) observatory (48.713 °N and 2.208 °E). The objective of the ParisFog campaign during three winters from 2010 to 2013 was to better understand the radiative, thermodynamic, dynamic and microphysical processes occurring during the fog life cycle. The site where the instrument platform was installed was a semi-urban area with mixed land cover including forest, lake, meadows and shrubs next to a built up area. As shown in Figure 1a, the instrumented zone was located near a forest area. Zaïdi et al. (2013) demonstrated the impact of the tree barrier on the observed flow when the wind was blowing from the barrier of trees over the instrument location, as in our case study. This fog case has previously been studied by Stolaki et al. (2015) using a 1D model.

Temperature and humidity sensors were located at heights between 1 and 30 m on an instrumented mast, with uncertainties of 0.2 K in temperature and 2% in relative humidity. Wind speed was measured by two ultrasonic anemometers at 10 m and 30 m above ground level (agl) on the same mast. Radiative fluxes were measured at a height of 10 m with $5\ \mathrm{W\,m^{-2}}$ and $4\ \mathrm{W\,m^{-2}}$ uncertainties for downward and upward fluxes respectively. Two diffusometers were operated at 3 m and 18 m to measure horizontal visibility with an uncertainty of up to 25%. Additionally, radiosondes were launched by Météo-France twice a day from Trappes (48.7°N, 2 °E), situated 15 km to the northwest of Sirta.

The microphysical instrumentation has been presented in detail by Mazoyer et al. (2016). A Fog-Monitor 100 (FM-100) provided the size distribution for particles 2 µm to 50 µm in diameter, and the particle diameter distribution was provided between 0.96 and 10 µm by a WELAS-2000 system.

Aerosol particle measurements were performed using a Scanning Mobility Particle Sizer (SMPS) measuring dry aerosol diameters between 10.6 and 496 nm every 5 min, and by a CCN chamber that gave the CCN number concentration at different supersaturations from 0.1 to 0.5% (Roberts and Nenes, 2005). An RPG-HATPRO water vapour and oxygen multi-channel

microwave profiler was used to measure the Liquid Water Path (LWP) with an error of up to $20\ \mathrm{g\,m^{-2}}$ (Lohnert and Crewell, 2003). Measurements of dewfall and fog-droplet deposition were not taken.

2.2 Presentation of the observed case

2.2.1 Dynamics and thermodynamics

Radiation fog formed at 0200 UTC on 15 November 2011 and dissipated at the ground around 1000 UTC on the following morning. Conditions favouring fog were due to a ridge at 500 hPa centred over the North Sea and anticyclonic conditions near the surface. One of the features of this event was the initial formation of a cloud layer at 150 m agl, followed 30 min later by fog occurring at the surface. As underlined by Stolaki et al. (2015), this characteristic is very common at Sirta and 88% of the radiation fog events during the field experiment followed a similar pattern. However, these events are not classified as stratus lowering as they were followed rapidly by formation of fog at the surface. A delay of 30 min between the formation at 150 m height and at the ground seems too short to be a stratus lowering, which is mainly driven by the evaporation of slowly falling droplets that cool the sub-cloud layer (Dupont et al., 2012). This suggests that this type of radiation fog could be linked with, and specific to, the configuration of the Sirta site.

The fog case is presented following the three phases of the fog life cycle defined by Nakanishi (2000). Before the fog onset, between 2200 and 0200 UTC, the surface boundary layer was stable and a near-surface cooling was observed, inducing an increase in relative humidity (Fig. 2). Between 0000 and 0130 UTC, the relative humidity (RH) near the ground remained nearly constant around 97%. Wind at 10 m height was light (speed around $1.8\ \mathrm{m\,s^{-1}}$) as was TKE, with small variability (Fig. 3). At 0200 UTC, the attenuated backscatter coefficient measured by the lidar increased significantly at 150 m agl (not shown), revealing the formation of liquid water at this height, while the RH at the surface remained at 97%. The cloud base height progressively subsided over the next 30 min, at which point it reached the ground. During this time, the near-surface temperature decreased by about 1 K in a stable stratification layer. At 0230 UTC, the appearance of fog at the ground was associated with a temperature homogenization in the first 30 metres, called temperature convergence by Price (2011) and corresponding to a neutral stratification. The downwelling longwave (LWD) radiation flux increased progressively to $325\ \mathrm{W\,m^{-2}}$ during the development of the fog layer (Fig. 4).

During the fog development and mature phases, between 0200 and 0700 UTC, the near-surface layer remained quasi-neutral and potential temperature at the different levels remained constant. The temporal variability of 10 m wind speed and TKE was greater during this period. Around 0400 UTC, TKE at 10 m height increased significantly, from 0.4 to $0.7\ \mathrm{m^2\,s^{-2}}$, and then presented some variability around this value. The vertical gradient of TKE between 30 m and 10 m remained positive. The sodar indicated that the fog top height reached a maximum of 300 m agl during the mature phase (Stolaki et al., 2015; Dabas et al., 2012).

At the beginning of the dissipation phase, starting at 0700 UTC, the surface temperature increased slowly (less than 0.5 K in 2 hours) and then more rapidly after 0900 UTC. At 1000 UTC, the downward SW fluxes exceeded $100\ \mathrm{W\,m^{-2}}$, while near-

surface temperature had increased by 1 K compared to the pre-sunrise values. TKE at 30 m decreased from 0800 UTC to 1000 UTC, while at 10 m, TKE remained approximately constant.

2.2.2 Microphysics

Measurements of microphysical properties near the surface indicated a sharp increase in cloud water mixing ratio (r_c) and droplet concentration (N_c) at the fog onset just after 0230 UTC (Fig. 5 in solid lines), reaching $N_c = 53\ \mathrm{cm}^{-3}$ and $r_c = 0.02\ \mathrm{g\,kg}^{-1}$. This corresponded to a drop in the near-surface visibility from 5000 m to less than 500 m (Fig. 6a in black line). The initial elevated structure of the fog led to an earlier decrease of the visibility at 18 m than at 3 m agl, with a time lag of the order of 30 min. Until 0730 UTC, r_c and N_c decreased slowly, inducing a small increase of the visibility at 3 m and 18 m (not shown). Between 0730 and 0800 UTC, cloud mixing ratio and droplet concentration at 3 m decreased strongly, allowing the visibility at 3 m to increase to 2000 m. At 18 m agl, the visibility remained less than 1300 m. The fog at the surface reformed just after 0800 UTC, reaching $N_c = 30\ cm^{-3}$ and $r_c = 0.02\ \mathrm{g\,kg}^{-1}$, with a visibility of less than 500 m, before definitively dissipating at 1000 UTC. The particle size distribution (PSD) indicated that 95% of the droplets had a diameter of less than 20 µm, meaning that there was probably a very small impact of the coalescence process. Sampled at 3 stages of the event, the PSD evolved during the fog life cycle and appeared consistent with the classification of Wendisch et al. (1998) (Fig. 5d). The "initial phase"(in red, at 0250 UTC) was characterized by a small droplet size but a broadening of the distribution between 8 and 12 µm was already visible, which persisted through the 3 stages. During the mature phase (in blue, at 0500 UTC), also called the "mass transfer stage", larger droplets, up to 22 µm, were more numerous. During the dissipation phase (in green, at 0700 UTC), the concentration of larger droplets fell but remained higher than during the initial phase.

The maximum LWP measured by the profiler was reached around 0730 UTC, at the beginning of the fog dissipation phase, with $70\ \mathrm{g\,m}^{-2}$ (Fig. 5c). The non-zero values ($5\ \mathrm{g\,m}^{-2}$) before the fog onset were within the error range of the measurement.

2.3 Model description

2.3.1 Presentation of the model

The non-hydrostatic anelastic research model Meso-NH (Lafore et al., 1998) (see http://mesonh.aero.obs-mip.fr) is used here in an LES configuration. The LES is based on a 3D turbulent scheme with a prognostic turbulent kinetic energy (TKE) (Cuxart et al., 2000) and a Deardorff mixing length (Deardorff, 1980).

The atmospheric model is coupled with the ISBA surface scheme (Interaction between Soil Biosphere and Atmosphere (Noilhan and Planton, 1989)) through the SURFEX model (Masson et al., 2013). This scheme simulates the exchanges of energy and water between the land surface (soil, vegetation and snow) and the atmosphere above it. It uses five prognostic equations for deep temperature, deep soil water content, surface temperature, surface soil water content and water interception storage by vegetation.

In order to consider the impact of trees at the instrumented site, we used the drag approach developed by Aumond et al. (2013) for a vegetation canopy. Both this study and Zaïdi et al. (2013) have shown that the drag approach gives better results

than the classical roughness law when reproducing the turbulence downstream of a forest area. The drag approach consists of introducing an additional term into the momentum and TKE equations as follows:

$$\frac{\partial \alpha}{\partial t}_{DRAG} = -C_d A_f(z) \alpha \sqrt{u^2 + v^2} \tag{1}$$

with $\alpha = u, v, TKE$, where u and v are the horizontal wind components, C_d is the drag coefficient, set to 0.2, and $A_f(z)$ is the canopy area density, representing the surface area of the trees facing the flow per unit volume of canopy. $A_f(z)$ is the product of the fraction of vegetation in the grid cell by the leaf area index (LAI) and by a weighting function representing the shape of the trees, as presented in Aumond et al. (2013). The trees introduced in the simulation domain for the land surface scheme correspond to Atlantic coast broad leaved trees.

The model includes a two-moment bulk warm microphysical scheme (Khairoutdinov and Kogan, 2000; Geoffroy et al., 2008), that considers droplet concentration N_c and mixing ratio r_c as prognostic variables for the fog. An additional prognostic variable N_{ccn} is used to account for already activated CCN, following the activation scheme of Cohard et al. (2000c). The aerosols are assumed to be lognormally distributed and the activation spectrum is prescribed as:

$$N_{ccn} = C {S_{max}}^k F(\mu, k/2, k/2+1, -\beta {S_{max}}^2) \tag{2}$$

where N_{ccn} is the concentration of activated aerosol, $F(a, b; c; x)$ is the hypergeometric function, C (m^{-3}) is the concentration of aerosols, and k, μ and β are adjustable shape parameters associated with the characteristics of the aerosol size spectrum such as the geometric mean radius ($\bar{r}$) and the geometric standard deviation (σ), as well as solubility of the aerosols (ε_m) and temperature (T) (see below for the values in our case study). S_{max} is the maximum of supersaturation for that grid box at a time step, corresponding to $\frac{dS}{dt} = 0$. The evolution of the supersaturation S includes three terms accounting for the effects of a convective ascent of vertical velocity w, the growth of droplets by condensation for the newly activated droplets, and radiative cooling, as in Zhang et al. (2014b):

$$\frac{dS}{dt} = \phi_1 w - \phi_2 \frac{dr_c}{dt} + \phi_3 \frac{dT}{dt}|_{RAD} \tag{3}$$

where $\phi_1(T)$, $\phi_2(T, P)$ and $\phi_3(T)$ are functions of temperature and pressure. Following Pruppacher et al. (1998) and after simplification, S_{max} can be diagnosed by:

$${S_{max}}^{k+2} . F(\mu, k/2, k/2+1, -\beta {S_{max}}^2) = \frac{\left(\phi_1 w + \phi_3 \frac{dT}{dt}|_{RAD}\right)^{3/2}}{2kc\pi\rho_w {\phi_2}^{3/2} B(k/2, 3/2)} \tag{4}$$

with B the Beta function and ρ_w the density of water. Thus, the aerosols potentially activated are exactly those with a critical supersaturation lower than S_{max}. The number of aerosols actually activated in a time step is the difference between the number of potentially activated aerosols and the number of aerosols previously activated during the simulation.

The condensation/evaporation rate is derived using the Langlois (1973) saturation adjustment scheme. Cloud droplet sedimentation is computed by assuming Stokes law for the cloud droplet sedimentation velocity and assuming that the cloud

droplet size distribution $n_c(D)$ fits a generalized Gamma law:

$$n_c(D) = N_c \frac{\alpha}{\Gamma(\nu)} \lambda^{\alpha\nu} D^{\alpha\nu-1} exp(-(\lambda D)^{\alpha}) \tag{5}$$

where λ is the slope parameter, depending on the prognostic variables r_c and N_c:

$$\lambda = (\frac{\pi}{6}\rho_w \frac{\Gamma(\nu+3/\alpha)}{\Gamma(\nu)} \frac{N_c}{\rho_a r_c})^{1/3} \tag{6}$$

α and ν are the parameters of the Gamma law, and ρ_a is the density of dry air. They were adjusted using droplet spectra measurements from the FM-100 database of our case study and were set at $\alpha = 1$ and $\nu = 8$. These parameters are also used for the radiative transfer.

In addition to droplet sedimentation, fog deposition is also introduced to represent direct droplet interception by the plant canopies. In the real world, it results from turbulent exchange of fog water between the air and the surface below, leading to collection (Lovett et al., 1997). In numerical weather prediction models (NWP), this process is not usually included, e.g. in the French NWP model AROME (Seity et al., 2011), the physics of which comes from Meso-NH. As fog deposition is a newly introduced process, only a simple formulation is considered for it here as a first step, in order to perform a sensitivity study. The fog deposition flux F_{DEP} is predicted at the first level of the atmospheric model (50 cm height) for grassy areas, and over the 15 m height for trees, in a simplistic way following Zhang et al. (2014b):

$$F_{DEP} = \rho_a \chi V_{DEP} \tag{7}$$

where $\chi = r_c, N_c$, and V_{DEP} is the deposition velocity. In a review based on measurements and parametrizations, Katata (2014) showed that V_{DEP} values ranged from 2.1 to 8.0 cms^{-1} for short vegetation. Here V_{DEP} is assumed to be constant, equal to 2 cms^{-1}. A test of sensitivity to this value is presented below. Water sedimentation and deposition amounts are input to the humidity storage of the surface model. A more complete approach in a further study would include a dependance of V_{DEP} on momentum transport as in von Glasow and Bott (1999) and also on LAI.

The radiative transfer is computed with the ECMWF radiation code, using the Rapid Radiation Transfer Model (RRTM, Mlawer et al. (1997)) for longwave radiation and Morcrette (1991) for shortwave radiation. Cloud optical properties for LW and SW radiation take account of the cloud droplet concentration in addition to the cloud mixing ratio. For SW radiation, the effective radius of cloud particles is calculated from the 2-moment microphysical scheme, the optical thickness is parametrized according to Savijärvi et al. (1997), the asymmetry factor is from Fouquart et al. (1991) and the single scattering albedo from Slingo (1989). For LW radiation, cloud water optical properties refer to Savijärvi et al. (1997).

2.3.2 Diagnostics of visibility

Visibility can be diagnosed assuming an exponential scattering law:

$$VIS = -\frac{ln\varepsilon}{\beta} \tag{8}$$

with β the extinction coefficient, and using a visual range defined by a liminal contrast ε of 0.02 (Koschmeider, 1924). Clark et al. (2008) used this equation to predict visibility correctly in an NWP model. The most common parametrizations used to diagnose the visibility from droplet properties in models employing 1-moment microphysical schemes can be expressed as:

$$VIS = \frac{a}{(\rho_a r_c)^b} \tag{9}$$

where a is 0.027 and b is 0.88 for Kunkel (1984) (units of r_c and VIS are $\mathrm{g\,kg^{-1}}$ and km respectively).

When droplet concentration N_c is taken into account with 2-moment microphysical schemes, the diagnostic becomes:

$$VIS = \frac{c}{(\rho_a r_c N_c)^d} \tag{10}$$

where c is 1.002 and d is 0.6473 for Gultepe et al. (2006) based on observations made in eastern Canada, and c is 0.187 and d is 0.34 for Zhang et al. (2014a) from measurements made in the polluted North China Plain.

Measurements of visibility can be employed to estimate the validity of the visibility diagnostics the most often used by models. The three formulations were applied to the observed r_c and N_c and compared to the observed visibility in order to determine which formulation fitted the observed values best (Fig. 6a). In our case study, Zhang et al.'s (2014a) parametrization was the most suitable, as it is more sensitive to low r_c and N_c values, even though it tends to underestimate the observed visibility slightly. Diagnostics from Kunkel (1984) markedly overestimated the 3 m observed visibility and the overestimation was worse with Gultepe et al.'s (2006) parametrization.

2.3.3 Simulation set-up

For the reference simulation (noted REF), the horizontal resolution is 5 m over a domain of 200 x 200 grid points. 126 vertical levels are used between the ground and the top of the model at 1500 m. The vertical resolution is 1 m for the first 50 m and increases slightly above this height. Momentum is advected with a fourth-order centred scheme (noted CEN4TH), whereas scalar variables are advected with the PPM (Piecewise Parabolic Method) scheme (Colella and Woodward, 1984). The time step is 0.1 s. The domain of simulation is presented in Figure 1b. It has a tree barrier 15 m high and 100 m wide perpendicular to the wind direction and the rest of the domain is composed of grass. The lateral boundary conditions are cyclic. The radiation scheme is called every second.

The simulation began at 2320 UTC on 14 November 2011 before the fog formation, and covered 12 h. Temperature, humidity and wind speed vertical profiles were initialized with data from the radiosonde launched from Trappes. Meteorological conditions at Trappes can differ slightly from those at the Sirta site. Therefore wind, temperature and humidity were modified in the nocturnal boundary layer up to 400 m agl to fit the data recorded at the 30 m meteorological mast at the Sirta site, as illustrated in Fig. A.1. The soil temperature and moisture were given by the soil measurements, corresponding to a surface temperature of 276 K and a soil moisture of 70%. Following the profiles from soundings, a geostrophic wind of $8\ m\,s^{-1}$ was prescribed, without any other forcing. To generate turbulence, a white noise of 0.5 K was applied in the first 100 m in addition to the effect of the trees.

It was also necessary to characterize the aerosol size spectrum for Eq. 2. The supersaturations reached in fog were lower than 0.1% meaning that the CCNC measurements were not directly usable, as shown by Hammer et al. (2014) and Mazoyer et al. (2016). However, by using the Kappa-Köhler theory and the SMPS observations, the aerosol concentrations at supersaturations under 0.1% can be retrieved if the aerosol hygroscopicity (κ) at these supersaturations is known. This method, proposed by Mazoyer et al. (2016), was applied to our case study in the hour before fog onset. Thus, above 0.1% supersaturation, the activation spectrum was found from observations and below 0.1% it was computed. This computed activation spectrum is fitted according to Eq. 2 (Fig. A.2a), which corresponds to the size distribution of aerosol particles ($C = 2017\ \mathrm{cm}^{-3}$, $\sigma = 0.424$, $\bar{r} = 0.1$,$\varepsilon_m = 1$) in red in Fig. A.2b. This does not match the measured distribution (in black) or the lognormal distribution fitted on the accumulation mode (in blue), because Cohard et al.'s (2000c) formulation was not developed for fog with low supersaturation. Deducing the activation spectrum from measurements provides the exact solution.

The reference simulation will now be presented.

3 The reference simulation

The performance of the REF simulation will first be examined, based on a comparison with observed values of thermohygrometric, dynamic, radiative and microphysical parameters near the ground. Considering that the REF simulation reaches good agreement with observation, the vertical evolution and horizontal variability of the simulated fog will be characterized during the different phases of the fog life cycle. It should be emphasized that observations localized at one point will be compared to simulated fields averaged over a horizontal area located downstream of the tree barrier (blue contour area of Fig. 1b), which is representative of the instrumented area. We will see that the simulation domain is divided into 4 parts with significant differences between them but with similar characteristics inside each one.

3.1 Parameters near the surface

3.1.1 Dynamics and thermodynamics

Figure 2a and c shows the time series of near-surface observed and simulated temperature and RH. At the initialization of the simulation, near-surface temperatures are in agreement with the observations while RH is very slightly underestimated. During the cooling before fog onset, the model develops a layer that is too stable, especially in the first 5 metres, between 0000 and 0100 UTC. The convergence of temperature is simulated with 30 minutes delay with respect to the observations

Considering RH near the surface (and the microphysical fields below), the fog starts to appear around 0200 UTC. Between 0430 and 0900 UTC, simulated and observed temperature are in fairly good agreement, with a quasi-neutral near-surface layer. The fog starts to dissipate from the ground at 0900 UTC, approximately one hour ahead of the local observation. This time discrepancy induces a slight overestimation of near-surface temperature, which is less than 0.5 K at 1100 UTC. Nevertheless, the negative temperature gradient near the surface representative of the development of the convective boundary layer is quite well reproduced after the beginning of the dissipation.

Dynamical fields at 10 m and 30 m are fairly well reproduced by the model (Fig. 3 in red): the 10 m wind speed (Fig. 3a) is in good agreement with observation throughout the simulation. Until 0300 UTC, a quasi linear increase of TKE is produced by the model with a higher TKE at 10 m agl than at 30 m contrary to observations (Fig. 3b). Around 0300 UTC, a more sudden increase of TKE occurs, as in the observations but 30 min before and with a lower magnitude. Then the simulated TKE remains almost constant around $0.7\ \mathrm{m^2\,s^{-2}}$ from 0400 UTC onwards, with a slightly higher variability than before. The model develops similar TKE values at 10 m and 30 m, while observed values are higher at 30 m.

Considering the radiative fluxes (Fig. 4), the increase of the LWD flux associated with fog onset is simulated with a delay of 30 minutes, meaning that there is a delay in the simulated formation of fog at elevated levels. After that, the LWD flux of $325\ \mathrm{W\,m^{-2}}$ is correctly reproduced, indicating that the temperature and the optical thickness of the fog are fairly well simulated. Observations develop a difference of $8\ \mathrm{W\,m^{-2}}$ between LWU and LWD during the fog life cycle, but the model fails to reproduce this difference, leading to a slight underestimation of LWU. If the measurements do not contain any errors, this probably means that the radiative properties of the simulated surface are not perfectly represented. A test on the emissivity of the surface (1 instead of 0.96) had no impact on the radiative fluxes, suggesting that the soil temperature was probably underestimated. After sunrise (0659 UTC), the downward and upward SW fluxes are overestimated up to $15\ \mathrm{W\,m^{-2}}$. LWD is slightly underestimated in a similar way due to the advanced dissipation time.

3.1.2 Microphysics

Considering the microphysical fields at 3 m agl, the onset of r_c higher than $0.001\ \mathrm{g\,kg^{-1}}$ is modelled 30 min early (Fig. 5a). Cloud droplets appear more than one hour before the observation but correspond to very low concentration (less than 10 per $\mathrm{cm^3}$) and negligible cloud mixing ratio. The delay identified on LWD flux increase and on the temperature convergence is not reproduced on r_c. This means that the time of formation of fog at the ground is quite correctly reproduced even with a small advance of 30 min but the previous formation at elevated levels is underestimated. This is corroborated by the LWP evolution (Fig. 5c), also characterized by a 30 min delay compared to the Sirta point observation, in agreement with LWD fluxes.

The increase of r_c during the development phase is too strong, leading to an estimated maximum value of $0.2\ \mathrm{g\,kg^{-1}}$ instead of the $0.03\ \mathrm{g\,kg^{-1}}$ observed. Then, during the mature phase, the slow decrease of r_c is reproduced, until 0900 UTC. However, as seen above, in reality this first event of fog dissipation only concerns the levels very close to the surface as observed visibility at 18 m remains less than 1300 m. In contrast, the fog does not reform near the surface in the simulation, which induces an advance of almost one hour on the dissipation time. The discrepancies between simulation and observation are greater on cloud droplet concentration than on cloud mixing ratio throughout the fog life cycle, as the model strongly overestimates N_c, by a factor that may be as high as 14 (maximum values of $700\ \mathrm{cm^{-3}}$ simulated against $53\ \mathrm{cm^{-3}}$ observed, Fig. 5b). Maxima of N_c and r_c are reached at the same time, around 0300 UTC, then r_c decreases while N_c remains constant, before N_c drops sharply at the end of the fog.

The droplet size distribution (DSD) in the model is described by the normalized form of the generalized gamma distribution which gives a monomodal form (Fig. 5d). During the whole fog life cycle, the model overestimates droplets that have a diameter larger than 4 µm and underestimates the smaller ones. The cloud water deposition rate at the ground presents a maximum of

$0.36\ \mathrm{mm\,day^{-1}}$ while the maximum of droplet sedimentation rate is $0.08\ \mathrm{mm\,day^{-1}}$. This means that deposition is the main contributor to the cloud water amount at the ground. A reason that could explain the overestimation of droplet concentration and that will be developed in Part 2 of this study, is that Eq. 3, which allows the supersaturation peak value to be computed, does not take the sink term due to pre-existing r_c into account, as explained by Thouron et al. (2012).

Due to the overestimation of simulated droplet mass and number, all the diagnostics of visibility applied to simulated microphysical fields underestimate the observed visibility at 3 m and 18 m, especially Zhang et al.'s (2014a) formulation (Fig. 6). As r_c is less severely underestimated than N_c, the Kunkel formulation provides the least bad match for observations. This explains why a simpler formulation of visibility based solely on r_c is usually more adequate given the difficulty of simulating N_c for the models.

The comparison between the REF simulation and observation for the set of parameters shows fairly good agreement, even though there are some discrepancies. The main discrepancies concerning the fog life cycle are an underestimation of the effect of elevated fog formation, inducing an advance of 30 min in the onset time near the ground and an advance of 1 h in the dissipation time. These elements are probably partly due to the semi-idealized representation of the Sirta surface in the simulation, and also to the comparisons with point observations, given the horizontal variability that we will see below. Considering the microphysical fields, the main discrepancy is an overestimation of the concentration of small droplets near the ground and, to a lesser degree, of the cloud mixing ratio. They are felt to be acceptable and we can therefore consider that the REF simulation can be used to explore the processes driving the fog life cycle and to conduct sensitivity tests to try to reduce these discrepancies.

3.2 Vertical evolution

First the vertical evolution of the fog is analysed. Figure 7 represents the time variations of vertical profiles of r_c and N_c, the radiative cooling rate and the vertical velocity in the updrafts, while parts a, c and d of Figure 8 represent the time variation for total turbulent kinetic energy (resolved plus subgrid, noted TKE), and dynamical and thermal production of TKE for the REF simulation, all averaged over the horizontal area downstream of the tree barrier. A first feature is that subgrid kinetic energy is one order of magnitude lower than resolved kinetic energy (not shown). This means that the 5 m horizontal resolution allows an LES approach as most of the eddies are resolved.

The evolution of r_c serves as a basis for decomposing the fog life cycle into the three phases: formation, between 0200 and 0300 UTC, until the fog becomes optically thick; development, between 0320 and 0820 UTC, until r_c at upper levels of the fog layer begins to decrease, and dissipation from 0820 UTC (Fig. 7a).

Before the fog onset and during the formation phase, the TKE is small and spread over a 30 m layer that deepens slowly because of the tree barrier (Fig. 8a). TKE mainly occurs by dynamical production, which presents maxima at two levels near the surface and at 15 m height due to the trees (Fig. 8c). Thermal production is negative because of the thermal stratification (Fig. 8d). Radiative cooling near the ground (Fig. 7c) and mixing by the tree drag effect are the ingredients that allow fog to appear at the same time over a 30 m deep layer (Fig. 7a). Then the mixing by the tree barrier causes the fog layer to develop vertically at greater heights (Fig. 7a). Hence, the effect of elevated formation is reproduced, even though the height of fog

onset is underestimated (150 m given by the ceilometer and 30 m in the simulation), and the fog subsides to reach the ground almost instantly. During this first phase, mean updraft vertical velocities are small, up to $0.15\ \mathrm{ms}^{-1}$ (Fig. 7d), in agreement with Ye et al. (2015), who observed a vertical velocity of $0.1-0.2\ \mathrm{ms}^{-1}$ in a fog layer between 40 m and 220 m deep in China. Considering Eq. 3 for supersaturation evolution with the two source terms depending on vertical velocity and radiative cooling, activation of fog droplets during the fog formation is mainly produced by radiative cooling at the top of the fog layer (Fig. 7b and c).

At the beginning of the development phase (around 0300 UTC), when the fog depth reaches approximately 80 m, it becomes optically thick to longwave radiation. At that time, TKE increases significantly by dynamical production (Fig. 8a and c), in agreement with Nakanishi's (2000) findings, which indicates a dynamical change. The optical thickness of the fog layer causes strong radiative cooling at the top of the layer, greater than $5.5\ \mathrm{Kh}^{-1}$ (in absolute value, Fig. 7c), and r_c values become stronger in the upper part of the fog layer. Hence, the fog top becomes the location of the dominant processes. Radiative cooling induces small downdrafts and buoyancy reversal. In addition to the vertical velocity of the updrafts, now higher than $0.2\ \mathrm{ms}^{-1}$ throughout the fog layer, a second maximum of droplet concentration of $1100\ \mathrm{cm}^{-3}$ occurs in the upper part of the fog layer around 0320 UTC. The sudden optical thickening corresponds to the increase of surface LWD to $320\ \mathrm{W\,m}^{-2}$ (Fig. 4) and to maximum cooling at the ground (Fig. 2a). At the same time, temperatures converge in the vertical levels near the ground, showing the effect of fog on the stratification as analysed by Price (2011).

During the development phase, the top of the fog layer is characterized by vertical wind shear inducing positive dynamical production of TKE, while small values of positive thermal production appear at the top due to buoyancy reversal. In the lowest 40 m of the fog layer, the drag effect of the trees induces values of kinetic energy higher than $0.6\ \mathrm{m}^2\mathrm{s}^2$. The maximum of r_c continues to increase in the upper part of the fog layer until 0500 UTC, reaching $0.37\ \mathrm{gkg}^{-1}$ at 120 m (Fig. 7a). At the same time, LWD surface fluxes remain constant while the fog layer continues to deepen and the LWP continues to increase until 0500 UTC (Fig. 5c).

Around 0500 UTC, a change occurs in the development of the fog layer: it continues to thicken, but at a slower rate, while the LWP begins to decrease in the simulation. This change of growth at the top of the fog layer is associated with a warming in the fog layer (not shown) and a decrease of the maximum radiative cooling near the top which spreads over a greater depth (Fig. 7c). This also corresponds to an increased number of resolved updraughts and downdraughts near the top (Fig. 7d). The variability of the fog depth also becomes stronger, in connection with fog-top waves as we will see below. This change of growth seems to be linked to the fact that the fog layer reaches the top of the nocturnal boundary layer, meeting stronger temperature, humidity and wind gradients. This increases the top entrainment process, limiting the deepening of the fog layer. With the decrease of top radiative cooling, cloud droplet concentration becomes more homogeneous in the fog layer, except near the ground where it decreases by deposition. The cloud mixing ratio also begins to decrease near the ground (Fig. 7b).

The beginning of the dissipation phase in the simulation (around 0820 UTC) is preceded by the beginning of solar radiation, and a divergence between surface LWU, which starts to increase, and surface LWD, which starts to decrease (Fig. 4). The dissipation of the fog begins at the surface, and the fog lifts into a stratus layer. The radiative heating of the surface induces the convective structure of the fog as vertical velocity in the updrafts increases (Fig. 7c and d) and thermal production of

TKE becomes significantly positive (Fig. 8d). Additionally, after sunset, downdraughts at the top of the fog layer increase the amount of solar radiation reaching the ground and feeding the heating at the base of the fog layer. Hence, near the ground, both thermal and dynamical effects contribute to the production of TKE, and to a deepening of the TKE layer to 60 m. The height of the fog top continues to increase as it is driven by radiative and evaporative cooling, which induces vertical motions and top entrainment. Although mixing ratio decreases at all levels, droplet concentration increases sharply when the fog layer lift from the surface (Fig. 7b). As the cloud evolves into a stratus layer, droplet activation is no longer induced by radiative cooling at the top of the fog layer but by updraft vertical velocity at all cloud depths, and especially near the stratus base. The stronger vertical velocity activates more droplets for the same water content. Droplets become smaller and more numerous, preventing the droplet sedimentation process and limiting the decrease of LWP. Moreover, the deposition process is no longer active as there are no cloud droplets at the surface. We will now consider the horizontal heterogeneity of the fog layer.

3.3 Horizontal variability

To better characterize turbulent structures and the impact of trees on the fog layer, the horizontal variability of the fog layer is examined. Figure 9 presents horizontal and vertical cross-sections of wind speed, cloud mixing ratio, potential temperature and TKE at 0210 UTC during the formation phase. The tree barrier tends to block the flow upstream. It enhances the turbulence by wind shear downstream, accelerating the flow near the ground and creating longitudinal structures in the direction of the wind. Ascents occur upstream and small subsidences downstream, up to $2\ \mathrm{cms}^{-1}$ (not shown). The subsidences bring warmer and dryer air from above to the ground. Therefore structures of stronger wind near the ground downstream of the trees coincide with structures of warmer, clear air as they delay fog formation. The fog forms at the surface upstream of the trees, and 500 m downstream, while it appears first at elevated levels over the intermediate area between the trees and downstream (Fig. 9d). The fog takes about 1 hour to cover the entire domain at ground level. Thus, heterogeneity of the surface vegetation explains heterogeneities in fog onset over the Sirta site, as well as the fog property of developing first at elevated levels. After the formation phase, the base of the fog layer is at the ground over the whole domain. These results are in agreement with the effects of buildings on fog studied by Bergot et al. (2015a) who found a 1.5 hour period of heterogeneity of fog formation over the airport area.

During the development phase, as shown on the vertical cross-sections of Fig. 10 at 0620 UTC, horizontal rolls appear at the top of the fog layer and are associated with dynamical production of TKE by shear. They are aligned almost perpendicularly to the mean wind direction (not shown). These structures correspond to Kelvin-Helmholtz (KH) instability, previously observed by Uematsu et al. (2005) and modelled by Nakanishi (2000) and Bergot (2013). They have depths corresponding to about one third of the fog layer height, as in Bergot (2013), and a horizontal wavelength of the order of 500 m. These horizontal rolls explain the oscillations at the top of the fog layer visible in Fig. 7 and Fig. 8. They become well marked from 0500 UTC when the increase in depth of the fog layer begins to slow down, as the fog layer reaches the top of the nocturnal boundary layer, meeting stronger wind gradients. The horizontal rolls induce strong horizontal variability of cloud mixing ratio near the top of the fog, with larger values in the ridges of the fog-top rolls, and smaller ones in the troughs (Fig. 10a). Local updraughts occur upstream of the crest of the wave, and downdraughts downstream, both up to $1.2\ \mathrm{ms}^{-1}$ (Fig. 10d). Maximum of droplet concentration

occurs near the top of the fog layer (Fig. 10b) in the radiative cooling layer (Fig. 10c), and preferentially upstream of the crest of the wave rather than downstream, in the ascent area, where the droplets are preferentially activated and transported. These extrema of droplet concentration do not appear in Fig. 7 as they are hidden by the spatio-temporal average.

Inside the fog layer, the radiative cooling is negligible while vertical velocity presents strong spatial heterogeneities. Maxima of supersaturation appear to be strongly correlated with vertical velocity (Fig. 10e), with values up to 0.25% which are probably overestimated, although this cannot be confirmed as measurements of supersaturation peaks are not available beyond the surface. However droplet concentration variations are smooth, and do not show a strong correlation with the maximum supersaturation, because of the pre-existing droplets.

Near the ground, maximum simulated values of supersaturation lie around 0.1% while Hammer et al. (2014) and Mazoyer et al. (2016) reported observed supersaturation peaks lower than 0.1%. The presence of trees and the deposition process induce a smaller droplet mixing ratio and concentration near the surface.

During the dissipation phase, heterogeneities remain at the top of the fog layer, but the signature of KH waves disappears (not shown). The dissipation of fog at ground level takes about 20 minutes, and, as noted in Bergot et al. (2015a), does not reveal a clear effect of surface heterogeneity.

Having characterized vertical and horizontal heterogeneities of the fog during its life cycle, sensitivity tests are now presented to identify the sources of variability and their impact on the microphysical fields.

4 Sensitivity study

In order to better characterize the physical processes dominating the fog life cycle and driving the microphysical properties, sensitivity tests were conducted in a second step. The resulting simulations and their differences relative to the REF simulation are summarized in Tab.1.

4.1 Impact of trees

To evaluate the impact of trees on the dynamics and on the microphysics of the fog, a simulation called NTR was run, in which the tree barrier was replaced by grass. So, deposition on the grass was considered over the whole domain. Fig. 3a shows that, without trees, the 10 m wind speed is overestimated over the instrumented area. As in REF but 30 min earlier, the model develops a sudden increase of TKE around 0230 UTC at the beginning of the development phase. This change is linked to the increase of the optical thickness and not to the turbulence induced by the trees (Fig. 3b and Fig. 8b). After this period, TKE is underestimated and remains stronger at 10 m height than at 30 m, contrary to observation. This means that the drag effect of trees is responsible for the observed stronger TKE at 30 m height. The fact that the REF simulation develops very similar TKE at 10 m and 30 m agl probably means that the representation of surface heterogeneities is still underestimated. This can be explained by the broad range of surface covers present in reality, in addition to the trees (lake, small buildings, etc.) but not included in the simulation.

The main differences in dynamics between NTR and REF appear first on total TKE, with a thinner layer of TKE values greater than $0.5\ \mathrm{m^2 s^{-2}}$ and smaller maxima (Fig. 8b). Before the fog formation, the too thin layer of turbulence near the ground in NTR limits the supply of warmer air from above. This induces an overestimation of the vertical temperature gradient before the fog, and emphasizes the cooling in the low levels, with 2 K less than in REF (Fig. 2b). Figure 11a presents the temporal evolution of cloud mixing ratio vertical profiles during the NTR simulation, to be compared to Fig. 7a for REF. Figure 12a and b show instantaneous vertical cross sections of potential temperature at the fog formation with REF and NTR. The stronger cooling with NTR homogenizes the fog formation at the ground and prevents elevated fog formation. The consequence is that the onset of fog with NTR occurs almost 2 hours earlier than actually observed and than in the REF simulation (Fig. 2d). Fig. 13 summarizes the impact of sensitivity tests on the microphysical fields and NTR (purple lines) can be compared to REF (red lines) in Fig. 13a b and c. During the formation and development phases, the fog layer is thinner in NTR than in REF. This is due to the formation at the ground and the absence of mixing without trees, thus limiting the vertical development. The maximum of cloud mixing ratio with NTR is increased compared to REF, due to the absence of warming by entrainment. It leads to largely overestimated cooling near the ground in comparaison to observations (Fig. 13a). Therefore the Kunkel diagnostic underestimates the visibility much more than REF, as do the other diagnostics (Fig. 6d). Inside the fog layer, despite the increase of r_c, the positive temporal evolution of N_c, called the production of N_c is not higher than in REF (Fig. 11b), as smaller vertical velocities and higher cloud mixing ratio production compensate for the stronger cooling in the activation process.

Additionally, near the ground, droplet concentration is even smaller than in REF: deposition, acting only at the first vertical level in NTR, is active from the onset of the fog, due to the absence of elevated formation and to the thinner fog layer. Consequently, the DSD at 3 m shifts towards larger droplets in NTR (Fig. 13c), consistently with the reduction of droplet concentration.

Also, during the development phase, 500 m wavelengths of KH waves are more smooth and regular without trees and this is noted during the whole phase. This is shown on kinetic energy spectra applied to vertical velocity over the whole fog depth, computed according to Ricard et al. (2013) and presented in Fig. 14. The spectra of REF and NTR present two main differences: firstly the TKE variance is smaller with NTR at wavelengths shorter than 200 m. This means that the flow presents fewer fine scale structures without the tree drag effect. Secondly, the peak of variance at 500 m wavelength, corresponding to the KH waves, is more pronounced in NTR.

To summarize, the absence of tree barrier produces an unrealistic simulation, as it causes the fog onset to occur too early (almost 2 hours in advance). It also induces cooling that is too strong in the low levels, and a large overestimation of the near-surface cloud mixing ratio throughout the fog life cycle, damaging the visibility. On the other hand, droplet activation is reduced near the ground due to smaller vertical velocities and to a stronger impact of surface deposition, shifting the DSD to larger droplets. The absence of trees also modifies the signature of the KH waves at the top of the fog layer, with a more regular pattern and fewer small scale heterogeneities. The impact of the deposition process will now be examined more precisely.

4.2 Impact of deposition

Three simulations were carried out to better characterize the role of the deposition process, all keeping the tree barrier. The first one, called NDT, removed only deposition over trees compared to REF, considering that trees acted as grass for deposition. This was done by activating deposition only at the first level of the model. The second one, called NDG, removed deposition altogether. The third one, noted DE8, considered a deposition velocity V_{DEP} of $8\ \mathrm{cm\,s^{-1}}$ over grass and trees, which is the upper bound given by Katata (2014) instead of $2\ \mathrm{cm\,s^{-1}}$ as in REF. Figure 13a, b and c compare 3 m microphysical fields, and Figure 15a the LWP.

NDT very slightly increases droplet mass and number downstream of the tree barrier, and the LWP during the fog life cycle (Fig. 15). Conversely, removing deposition everywhere with NDG has a considerable impact as it increases the near-surface cloud mixing ratio and concentration by a factor between 2 and 3. With NDG, the onset of fog occurs at the surface and not on a 30 m deep layer, almost 2 hours earlier than in observations and in the REF simulation (Fig. 11c). During the development phase, there is no longer a vertical gradient of r_c and N_c (Fig. 11c and d). The temporal evolution of cloud droplet concentration in the fog layer shows constant vertical profiles, without maxima during the formation and the dissipation phases, as in REF. Hence, cloud droplet concentration is constant during the fog life cycle near the ground, while observations report a decrease during the development phase (Fig. 13b). NDG also develops a broader DSD, with more droplets having a diameter larger than 4 µm.

The fog layer is deeper throughout the life cycle, and therefore the LWP is largely overestimated with a maximum between 0500 and 0600 UTC, of about twice the observed value (Fig. 15). Due to the larger amount of cloud water near the ground, the dissipation at the ground is delayed by more than one hour. Moreover, NDG reports a 12 hours surface maximum cumulated cloud water amount of 0.053 mm produced by droplet sedimentation, while the REF simulation gives a maximum of 0.074 mm by deposition and sedimentation. Even if NDG produces higher LWP over a longer period and higher concentration of large droplets than REF, the cloud water amount reaching the ground is lower. This means that a deposition velocity of $2\ \mathrm{cm\,s^{-1}}$ is more efficient than the sedimentation process to collect cloud water at the ground.

In contrast, DE8 induces a significant reduction of the near-surface r_c, N_c and LWP, and the onset of fog near the ground coincides relatively well with observation. The formation of fog at elevated levels is more pronounced, and r_c over the whole fog depth is reduced during the development phase compared to REF (Fig. 11d and e). With DE8, the cloud water deposition rate at the ground presents a maximum of $0.48\ \mathrm{mm\,day^{-1}}$ during the period while the maximum of droplet sedimentation rate is $0.02\ \mathrm{mm\,day^{-1}}$. Among the different simulations conducted in this study, DE8 performs best to reproduce the microphysical fields. This means that the deposition process is highly sensitive to the deposition velocity.

Zhang et al. (2014b) have already shown that including a deposition term in simulations seems to have some effect on the droplet concentration in the layer near the ground and consequently on visibility. However, the effect they found was less pronounced than the one seen here. A possible explanation is that both $u*$, the friction velocity, and the mean volumetric diameter of droplets used in their parametrization, were underestimated. In our case, the deposition process, even with a simple parametrization, appears to be essential to correctly simulate the fog life cycle and to approach the observed microphysical

values near the ground more closely. It impacts the microphysical fields significantly. Hence, neglecting this process increases droplet sedimentation but in insufficient quantity to avoid unrealistic droplet concentration and cloud mixing ratio in the fog layer and near the surface. It also modifies the fog life cycle in terms of onset and dissipation times, LWP and microphysical characteristics inside the fog layer. The elevated fog formation, which is a climatological characteristic of the Sirta site, is the result of two effects: the tree drag effect, which mixes the lowest levels, and the deposition process, which erodes the near-surface water content. We will now examine the impact of the horizontal resolution on the simulated fog life cycle.

4.3 Sensitivity to effective resolution

In order to assess the impact of spatial resolution on the fog life cycle, a 2 m horizontal resolution simulation (called DX2) was carried out using the same momentum advection scheme as in REF (CEN4TH). According to Skamarock (2004), kinetic energy (KE) spectra deduced from simulations allow the effective resolution to be set up as the scale at which the model starts to depart from the theoretical slope, which is -3 for vertical velocity spectra applied to stable turbulence. Mean KE spectra applied to the vertical wind component reveal effective resolution of the order of $4-5\ \Delta x$ for simulations with CEN4TH (DX2 and REF), in agreement with Ricard et al. (2013), namely 8 m and 20 m respectively (Fig. 14).

With DX2, top entrainment is more active as updrafts and downdrafts are represented at finer resolution, limiting the cooling near the surface (Fig. 12d) and the vertical development of the fog. The cloud mixing ratio near the ground is slightly reduced, but the droplet concentration is almost unchanged, inducing a shift of the mode of the DSD to 7 µm instead of 8 µm (Fig. 13d, e and f).

The fog onset time occurs slightly later and the dissipation time sooner (Fig. 13e), and the LWP is slightly reduced compared to REF (Fig. 15b). But the differences between DX2 and REF remain quite small in agreement with the convergence around 2 m resolution in stable conditions shown by Beare and MacVean (2004).

In two other tests performed on the wind transport scheme, keeping the 5 m horizontal resolution, the CEN4TH scheme was replaced by the WENO (Weighted Non-Oscillatory, Shu (1998)) scheme at 3rd order (called WE3) or 5th order (called WE5). These spatial schemes, associated with an Explicit Runge-Kutta temporal scheme, allow time steps 10 times larger than CEN4TH associated with a Leap-Frog temporal scheme, but they were run here with the same small time step (0.1 s) for comparison. Due to the upstream spatial discretization, WENO schemes are implicitly diffusive and are therefore characterized by a coarser effective resolution, especially WENO3 because of its lower order. Fig. 14 shows that the effective resolutions are 35 m (i.e. 7 Δx) and 70 m (i.e. $14\ \Delta x$) for WE5 and WE3 respectively.

WE3 significantly reduces the top entrainment and the supply of warmer, dryer air from above. This emphasizes the cooling near the surface (Fig. 12c) as the diffusive contribution of the advection operator dissipates small updrafts and suppresses part of the resolved kinetic energy variance, in particular that present at the top of the fog layer. This induces an overestimation of the thermal gradient near the surface before the fog, and leads to cooling that is too strong by 1 K during the fog (not shown). The consequences of the increased cooling are that the onset of fog at the surface occurs 1.5 h earlier than actually observed, the r_c is largely overestimated throughout the fog life cycle, and the dissipation is delayed (Fig. 13e). The DSD is characterized

by higher concentrations of larger droplets (Fig. 13f). Considering the microphysical fields, WE3 tends to be closer to NTR simulation, meaning that a diffusive transport scheme significantly diminishes the tree drag effect.

In contrast, the differences between WE5 and REF are very small: only the LWP is higher with WE5 during the dissipation phase due to a slightly deeper fog layer. This underlines the less diffusive behaviour of WENO5 and its higher accuracy compared to WENO3.

Thus the jump in the effective resolution with the diffusive WENO3 scheme affects the fog life cycle significantly, while the smaller deviation with WENO5 has almost no impact. Increasing numerical implicit diffusion seems to have almost the same effect as removing the drag effect of trees. This also underlines the importance of the numerical schemes for correct handling of the cloud edge problem (Baba and Takahashi, 2013).

5 Conclusion

Large eddy simulations of a radiation fog event observed during the ParisFog campaign were performed, with the aim of studying the impact of dynamics on microphysics. In order to study the local structures of the fog depth, simulations were performed at 5 m resolution on the horizontal scale and 1 m on the vertical scale near the ground, and included a tree barrier present near the instrumented site, taken into account in the model by means of a drag approach. The model included a 2-moment microphysical scheme, and a deposition term was added to the droplet sedimentation, representing the interception of droplets by the plant canopies and acting only at the first vertical level above grass, and above the height of the trees.

The performance of the reference simulation was satisfactory as it gave fairly good agreement with the classical near-surface measurements. The main discrepancies were an overestimation of the concentration of small droplets near the ground, an overestimation of liquid water content, and an advance of one hour in the dissipation time. This good performance allowed the processes driving the fog life cycle to be explored.

The formation of the fog at elevated levels and the fact that it subsided to the ground in a very short time, a frequently observed characteristic of radiation fog events at the Sirta site, has been explained. It is a consequence of the tree drag effect when the wind meets this obstacle and the deposition effect, which reduces the formation of droplets near the surface. In contrast, the fog formed at the surface first upstream and 500 m downstream of the trees, leading to a duration of about one hour for fog formation at the surface over the whole domain.

At the beginning of the development phase, the fog became optically thick to longwave radiation, inducing a significant increase of kinetic energy by dynamical production, which was also associated with temperature convergence at low levels. The radiative cooling near the top of the fog layer was the main source of droplet activation so the droplet concentration was maximum in the upper levels of the cloud.

During the development phase, the fog layer depth grew more slowly when the fog reached the top of the nocturnal boundary layer, encountering stronger thermodynamical gradients and wind shear. Horizontal rolls at the top of the fog layer, associated with Kelvin-Helmholtz instabilities, became prominent. The cloud droplet concentration became quasi homogeneous in the fog layer when averaged over time but extremes of droplet concentration occurred locally near the top of the fog in the radiative

cooling layer, with maxima preferentially upstream of the crests of the waves rather than downstream, in the ascent area. This indicates that vertical velocity makes the main contribution to droplet activation at the top of the fog layer, followed by the contribution of radiative cooling. Inside the cloud layer, maxima of supersaturation were directly linked to the local updrafts, while variations of droplet concentration were smoother.

During the dissipation phase, as the fog evolved into a stratus layer, the cloud mixing ratio decreased at all levels. However, a sharp increase in the droplet concentration occurred over the whole depth of the cloud because droplets were now only activated by the convective ascents.

Various sensitivity tests allowed the main processes affecting the evolution of fog to be identified. The tree drag effect and the deposition process were considered as essential to correctly reproduce the main characteristics of the fog. The absence of the tree barrier produced an unrealistic fog simulation, with too early an onset, excessively strong cooling and a large overestimation of the near-surface r_c, worsening visibility diagnosis.

Neglecting the deposition process over the whole vegetation canopy exerted the most significant impact on the fog prediction. It produced more unrealistic near-surface water content, prevented elevated fog formation, and also modified the fog life cycle and suppressed vertical and temporal heterogeneities of the microphysical fields. Conversely, increasing the droplet deposition velocity from $2\ \mathrm{cm s^{-1}}$ to $8\ \mathrm{cm s^{-1}}$ significantly reduced the cloud mixing ratio near the surface and the droplet concentration. Increasing the horizontal resolution to 2 m did not change the fog prediction significantly, which means that grid convergence seems to be achieved at these resolutions. Conversely, increasing the numerical diffusion with a momentum transport scheme of lower order, involving a coarser effective resolution, drastically limited the top entrainment, and tended strongly towards the solution where the tree drag effect was ignored. This underlined the importance of the properties of numerical schemes in LES, particularly at cloud edges.

Other tests, not presented here, modifying the initial conditions in terms of humidity or wind profiles, impacted the fog life cycle but failed to reduce the overestimated droplet number concentration. This means that taking away some humidity in the initial state did not reduce the droplet concentration. The overestimation of the droplet concentration could not be explained by an inadequate initial humidity profile.

This study demonstrates the feasibility and the interest of LES including surface heterogeneities to improve our understanding of fog processes. At these fine resolutions, surface heterogeneities have a strong impact, explaining part of the variability in the fog layer and making these simulations very challenging. Therefore, horizontal and vertical variabilities of the fog layer also need to be more thoroughly explored in future field experiments. The horizontal variability, especially at the onset of the fog, also stresses that one point observation may not be very representative of what happens over a coarser grid box of a numerical weather prediction model.

One of the main points of this study is that fog water deposition should not be neglected in 3D fog forecast models, as still often occurs. It influences not only microphysical fields near the ground but also the whole fog life cycle. It seemed to be more important than droplet sedimentation in our case, bearing in mind that this observed case was characterized by small droplet concentrations and cloud mixing ratio. In this study, the deposition term was introduced quite crudely and this would need some refinements in further studies. It would need to take account of the wind speed and the turbulence, and it could also consider the

hygroscopic nature of canopies. By analogy with dry deposition, it would also be better to take droplet diameter into account, assuming that this field is correctly reproduced. Other studies have also shown that fog water deposition is strongly enhanced at the forest edge, becoming up to 1.5-4 times larger than that in closed forest canopies (Katata, 2014), so it could be interesting to simulate the edge effect of fog water deposition. It is also crucial to perform measurements of fog water deposition and dewfall during field experiments (Price and Clark, 2014).

This study has shown the great importance of some dynamical effects operating at first order for correct predictions of the fog life cycle. Despite the number of tests carried out, none succeeded in correctly reproducing the droplet concentration, which is always overestimated. Now that the fog life cycle has been correctly reproduced on this case, trying to correct this defect appears to be the main priority. Thouron et al. (2012) have developed a new scheme based on a supersaturation prognostic variable to avoid excessive droplet concentration in 2-moment microphysical schemes, as they have demonstrated that some assumptions of the adjustment process are no longer valid with LES. One of the main points is that the pre-existing cloud water should be taken into account as a sink of supersaturation, in order to limit the activation of cloud droplets. The relevance of this scheme, applied in Thouron et al. (2012) to cumulus and stratocumulus clouds, needs to be demonstrated for fog clouds, and this will be the subject of the second part of this study.

Acknowledgements. The authors are very grateful to all SIRTA operators and database managers. This research was partially funded by the European Community's Seventh Framework Programme (FP7/2007-2013) under the SESAR WP 11.2.2 project (Grant Agreement 11-120809-C)

Name ofsimulation	Difference of configuration with REF
NTR	No TRee: homogeneous surface
NDT	No Deposition on Trees
NDG	No Deposition (on Grass or trees)
DE8	Deposition velocity equal to $8\ \mathrm{cm\,s^{-1}}$
DX2	Horizontal resolution = 2m
WE3	3rd order WENO advection for momentum
WE5	5th order WENO advection for momentum

Table 1. Simulation configurations for sentivity tests

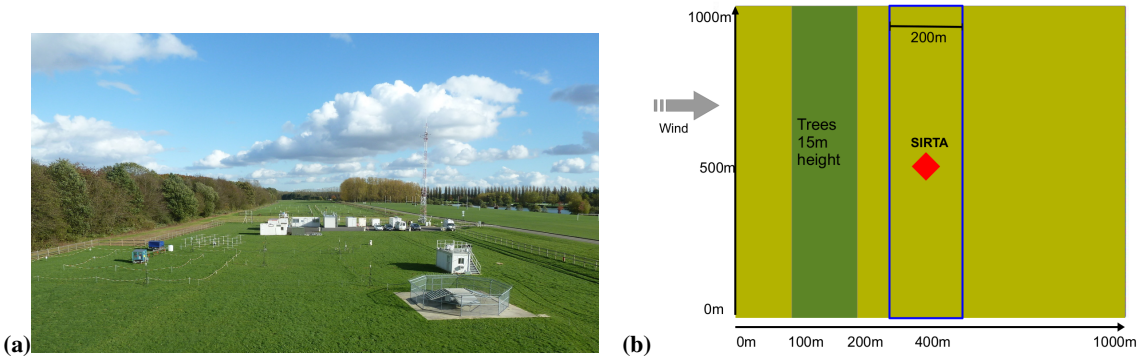

Figure 1. View of the measurement site (a) and modelling domain (b) with the tree barrier. All the simulated averaged results are presented in the blue contour area.

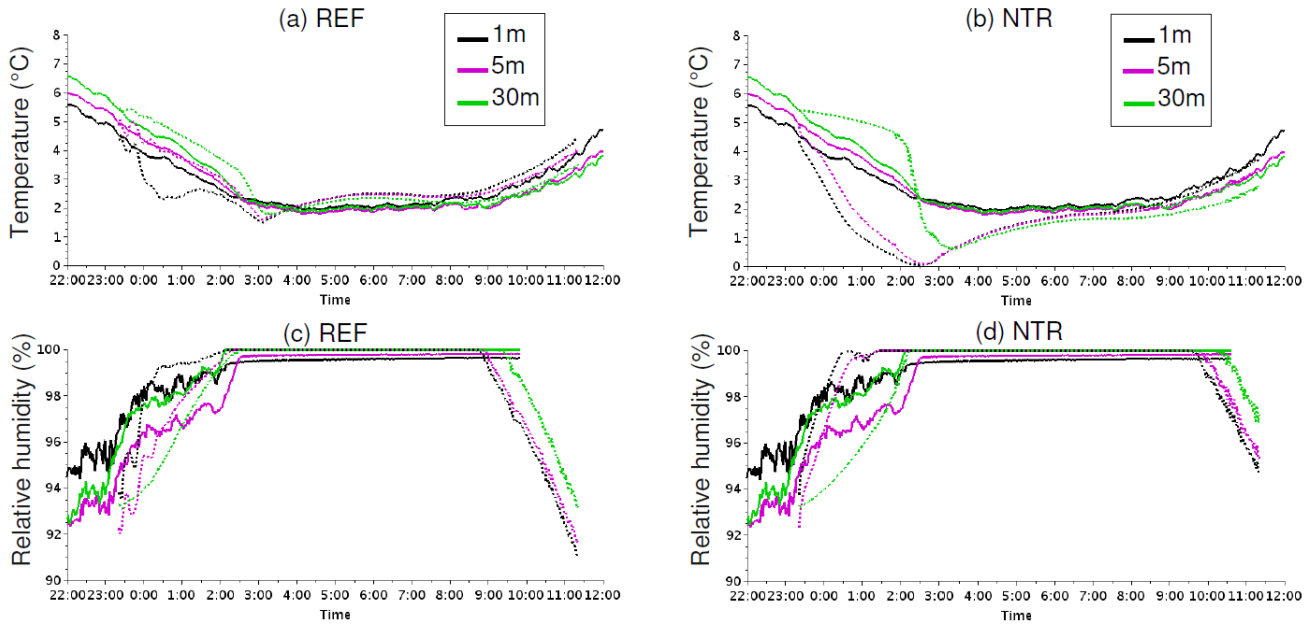

Figure 2. Observed (solid lines) and simulated (dashed lines) temporal evolution of temperature (a and b) and relative humidity (c and d) at 1m, 5m and 30m for the REF (a and c) and the NTR (without trees) (b and d) simulations. Simulated fields are averaged over the horizontal area located downstream of the tree barrier (blue contour area of Fig. 1b).

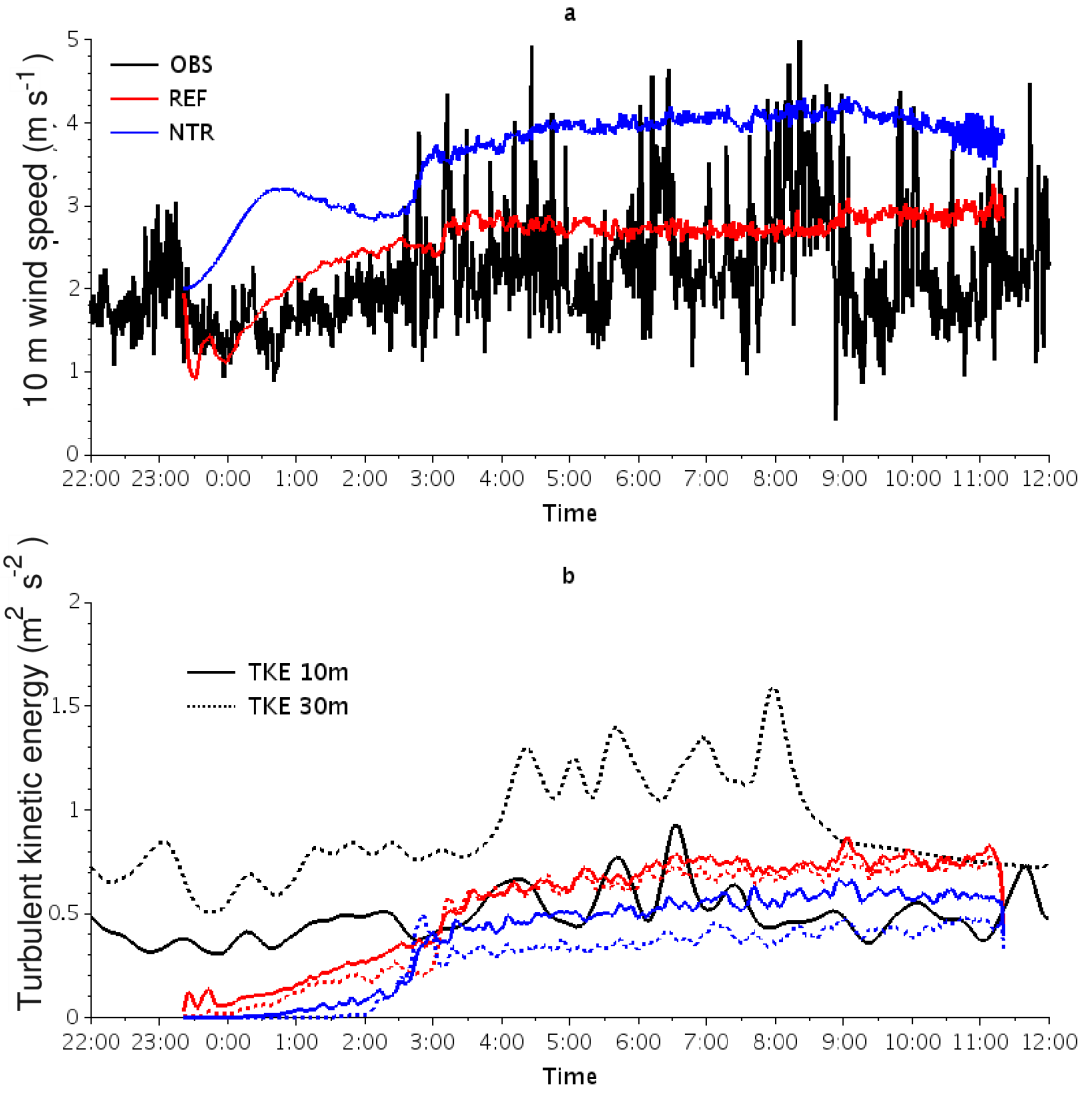

Figure 3. Observed (black lines) and simulated (coloured lines) temporal evolution of 10m wind speed (a), 10m TKE (solid line) and 30m TKE (dotted line) (b) for the REF (red line) and the NTR (without trees) (blue line) simulations. Simulated fields are averaged over the horizontal area located downstream of the tree barrier (blue contour area of Fig. 1b).

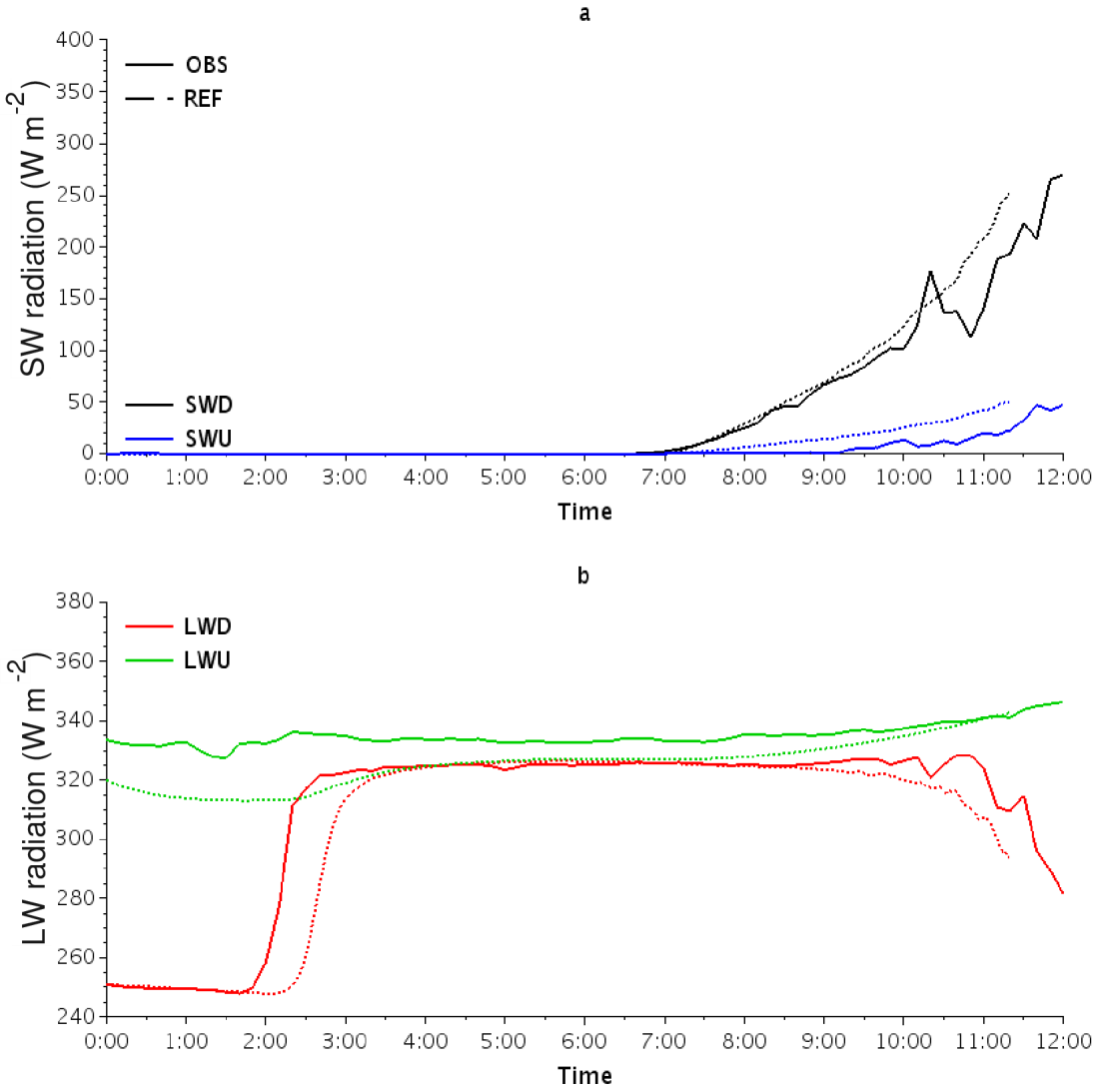

Figure 4. Observed (solid lines) and simulated (dotted lines, with the REF simulation) temporal evolution of downward and upward (at 1m) shortwave (a) and longwave (b) radiation fluxes (in W/m^2). Simulated fields are averaged over the horizontal area located downstream of the tree barrier (blue contour area of Fig. 1b).

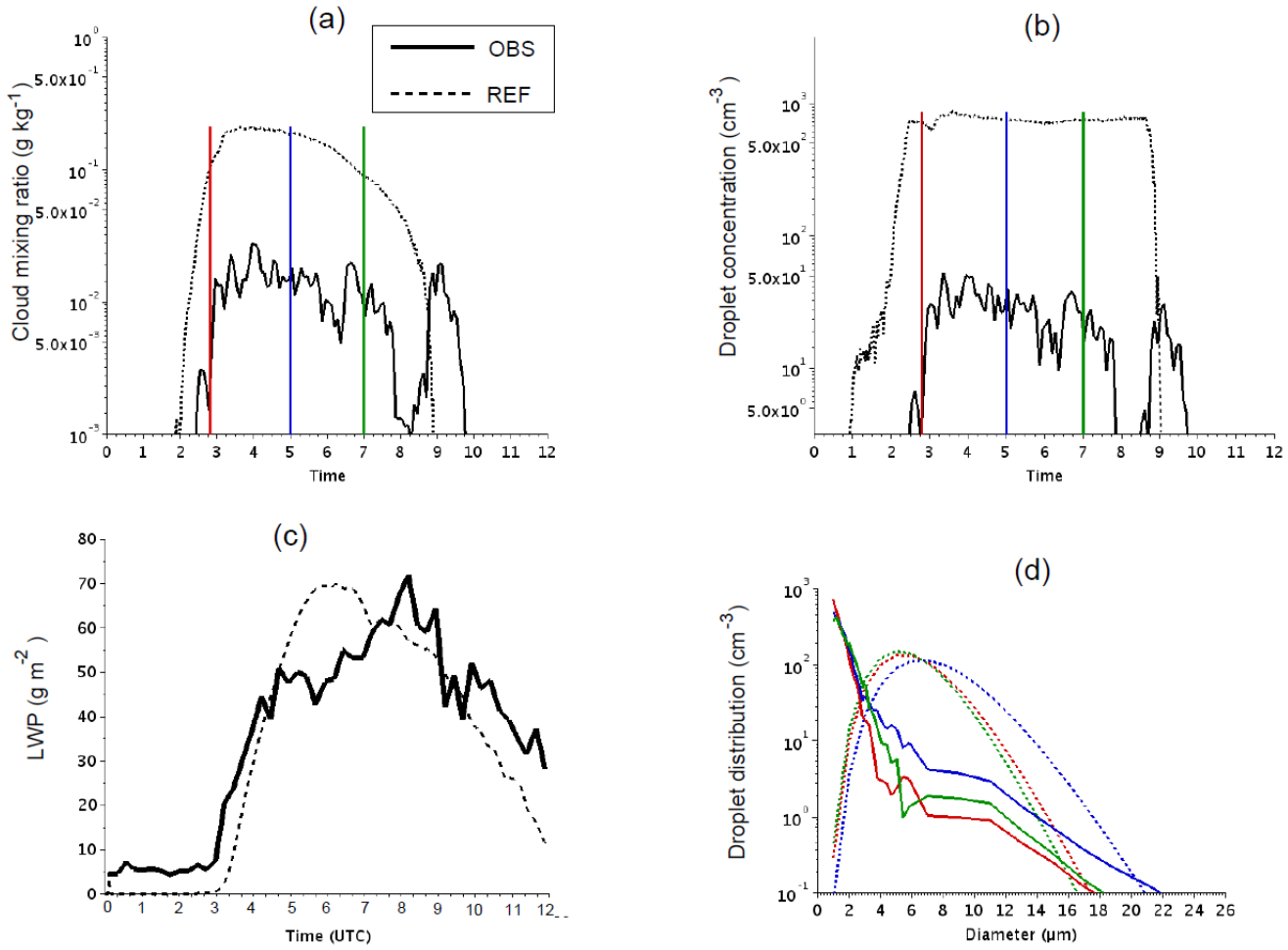

Figure 5. Time series of cloud mixing ratio (a, in $\mathrm{g\,kg^{-1}}$), droplet concentration (b, in $\mathrm{cm^{-3}}$), LWP (c, in $\mathrm{g\,m^{-2}}$), and particle size distribution (d, in $\mathrm{cm^{-3}}$) at 0250 UTC (in red), 0500 UTC (in blue) and 0700 UTC (in green) at 3 m agl observed (solid line), and simulated by REF (dotted line). Simulated fields are averaged over the horizontal area located downstream of the tree barrier (blue contour area of Fig. 1b).

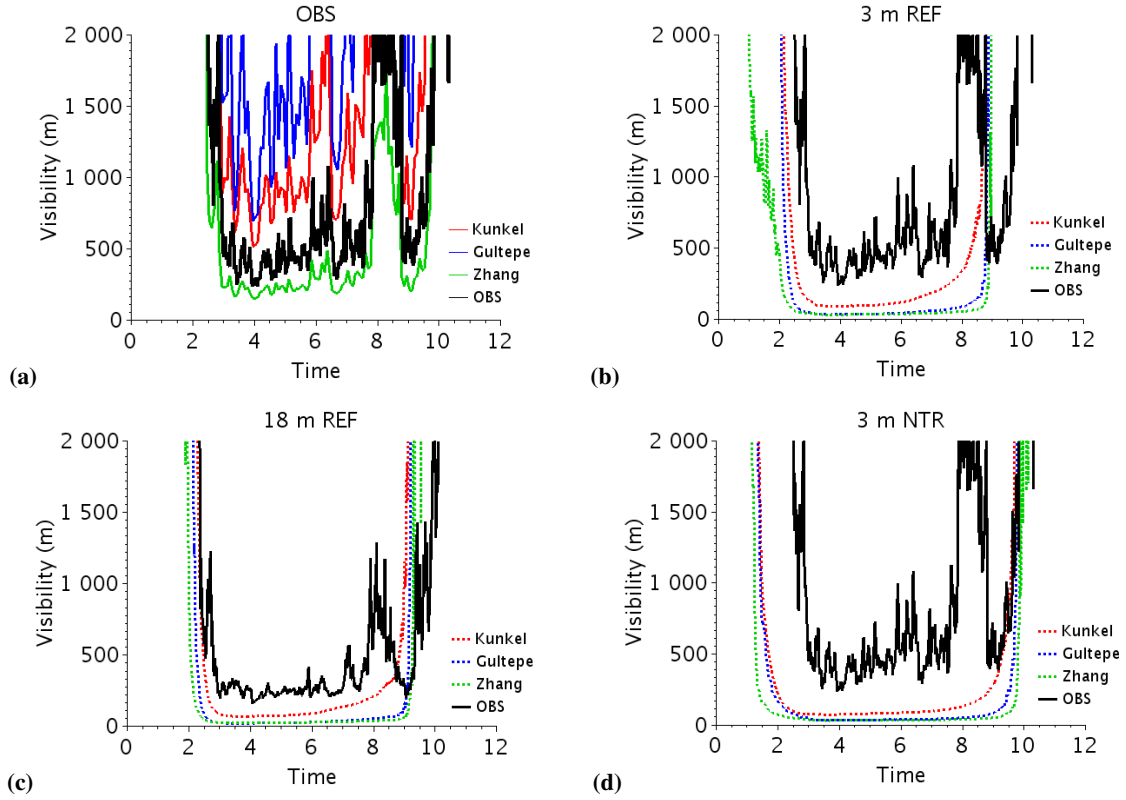

Figure 6. (a) 3 m observed (in black) and diagnosed (in colour) visibility with the observed microphysical fields according to Kunkel (1984); Gultepe et al. (2006); Zhang et al. (2014a) (in m). (b) and (c) 3 m and 18m visibility diagnosed with the microphysical fields from the REF simulation. (d) 3 m visibility diagnosed with the microphysical fields from the NTR simulation (in m). Diagnosed visibility from simulations uses averaged microphysical fields over the horizontal area located downstream of the tree barrier (blue contour area of Fig. 1b).

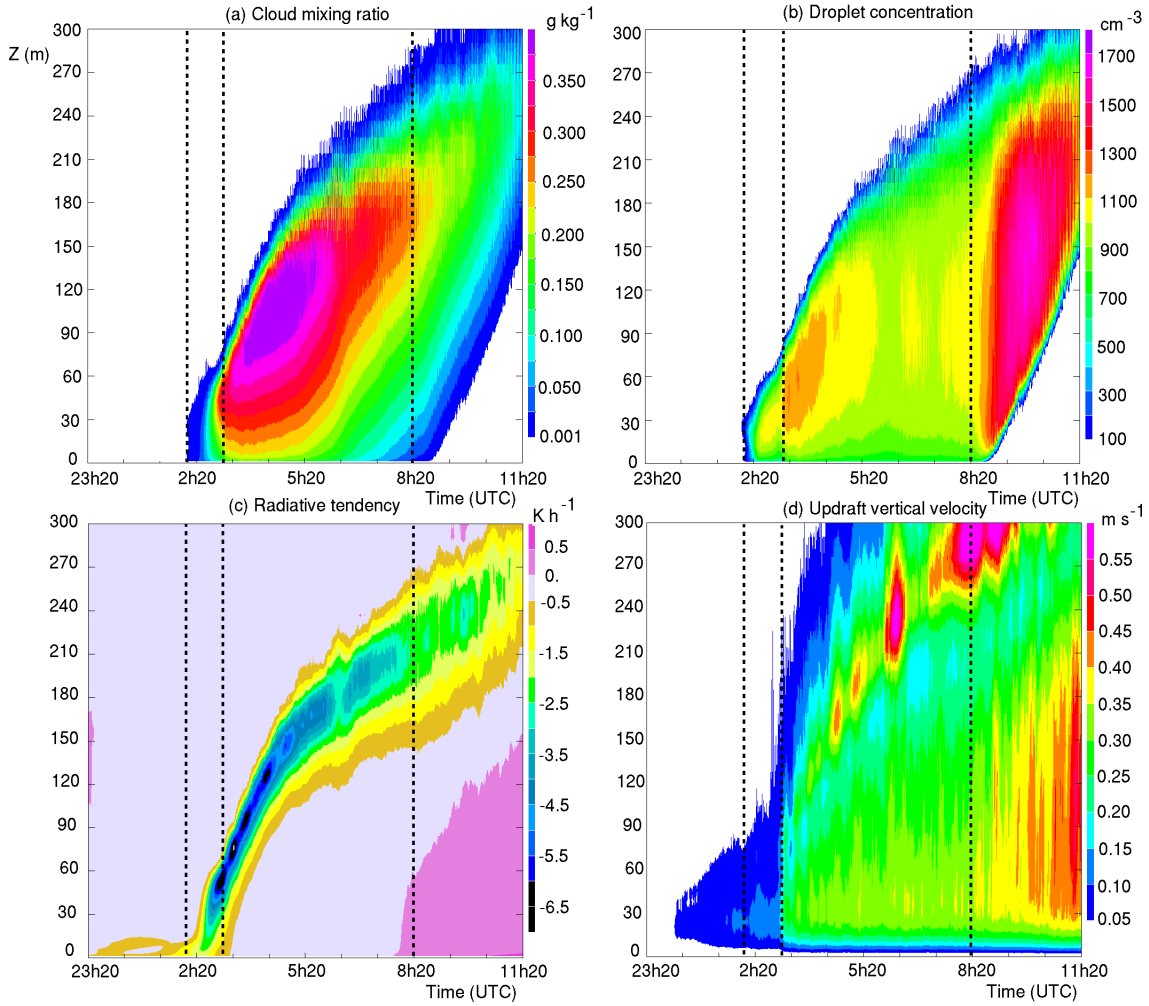

Figure 7. Temporal evolution of simulated vertical profiles of cloud mixing ratio (a, in $\mathrm{g\,kg^{-1}}$), droplet concentration (b, in $\mathrm{cm^{-3}}$), radiative tendency (c, in $\mathrm{K\,h^{-1}}$) and updraft vertical velocity (d, in $\mathrm{m\,s^{-1}}$) for the REF simulation. Fields are averaged over the horizontal area located downstream of the tree barrier (blue contour area of Fig. 1b). The three phases of the fog life cycle are delimited by dotted lines.

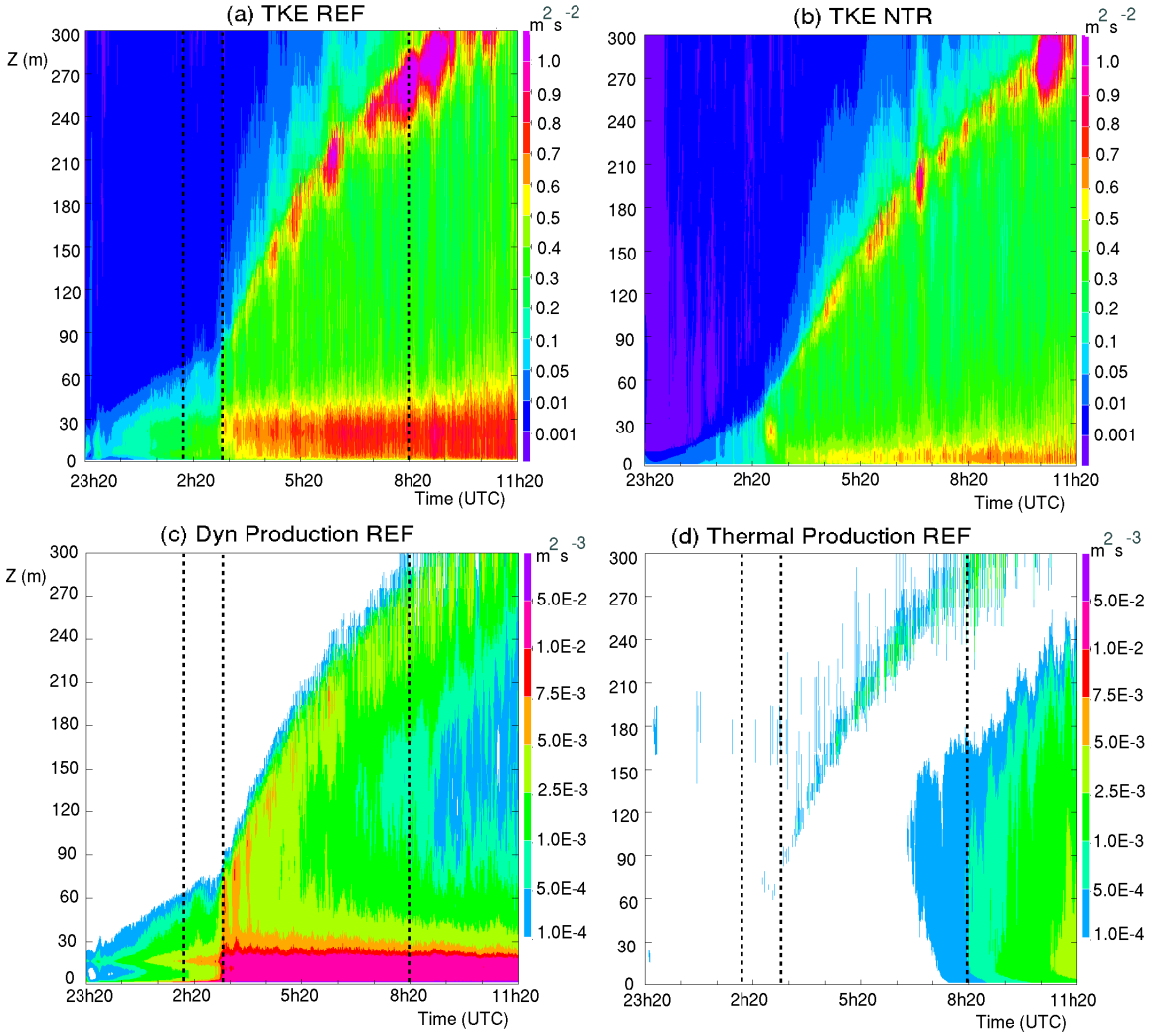

Figure 8. Temporal evolution of mean vertical profiles of total (resolved+subgrid) turbulent kinetic energy (in $m^2\,s^{-2}$) for REF (a) and NTR (b) simulations, and dynamical (c) and thermal (d) production of total turbulent kinetic energy (in $\mathrm{m^2\,s^{-3}}$) for the REF simulation. Fields are averaged over the horizontal area located downstream of the tree barrier (blue contour area of Fig. 1b). The three phases of the fog life cycle are delimited by dotted lines.

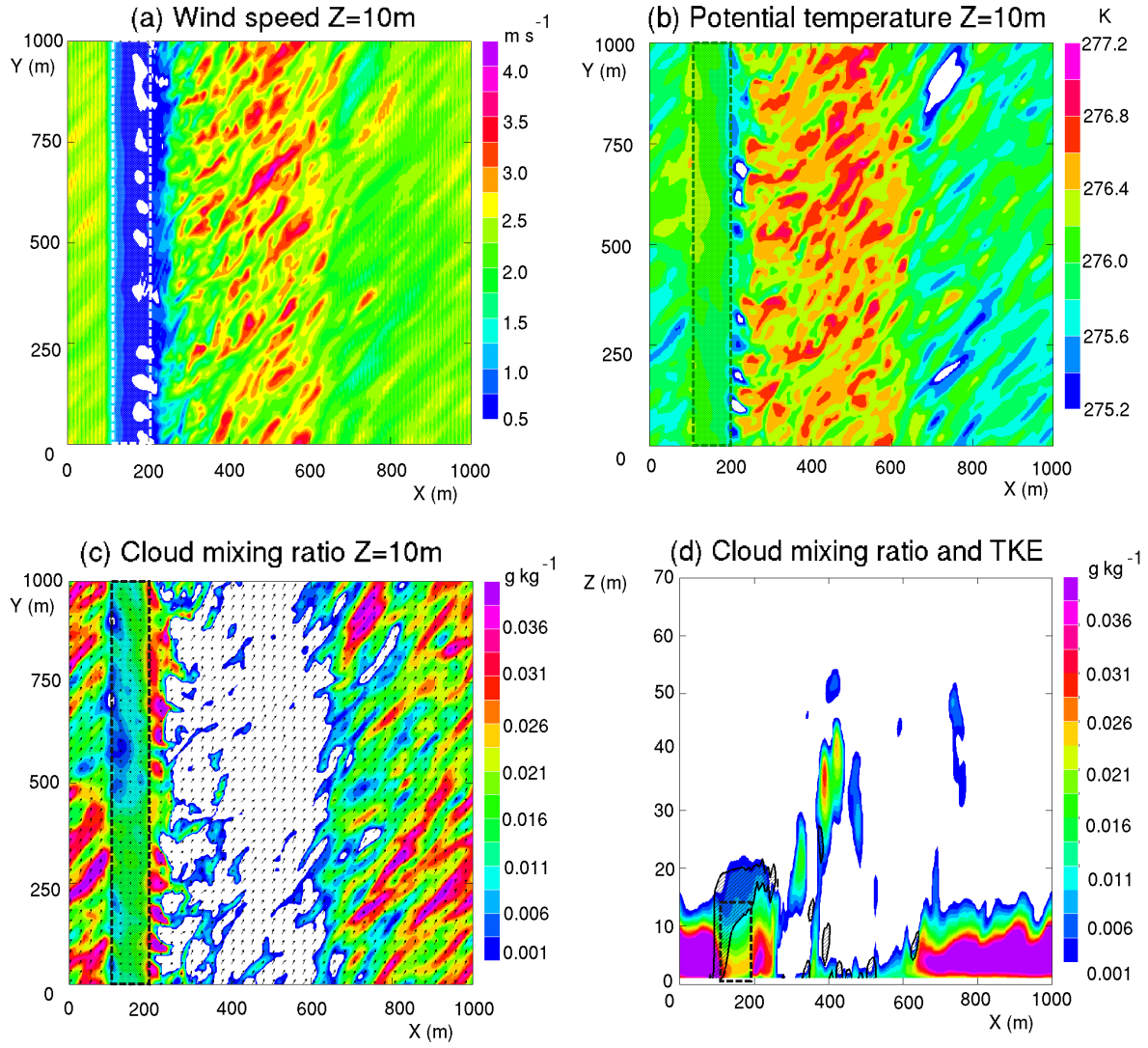

Figure 9. REF simulation at 0210 UTC: (a), (b) and (c): Horizontal cross-section at 10 m height of wind speed (a, in $\mathrm{m\,s^{-1}}$), potential temperature (b, in K) and cloud mixing ratio (c, in $\mathrm{g\,kg^{-1}}$). (d): Vertical cross-section at Y=500m of cloud mixing ratio (in $\mathrm{g\,kg^{-1}}$) with area of TKE higher than $0.1\ \mathrm{m^2\,s^{-2}}$ shaded. The barrier of trees is marked with a rectangle.

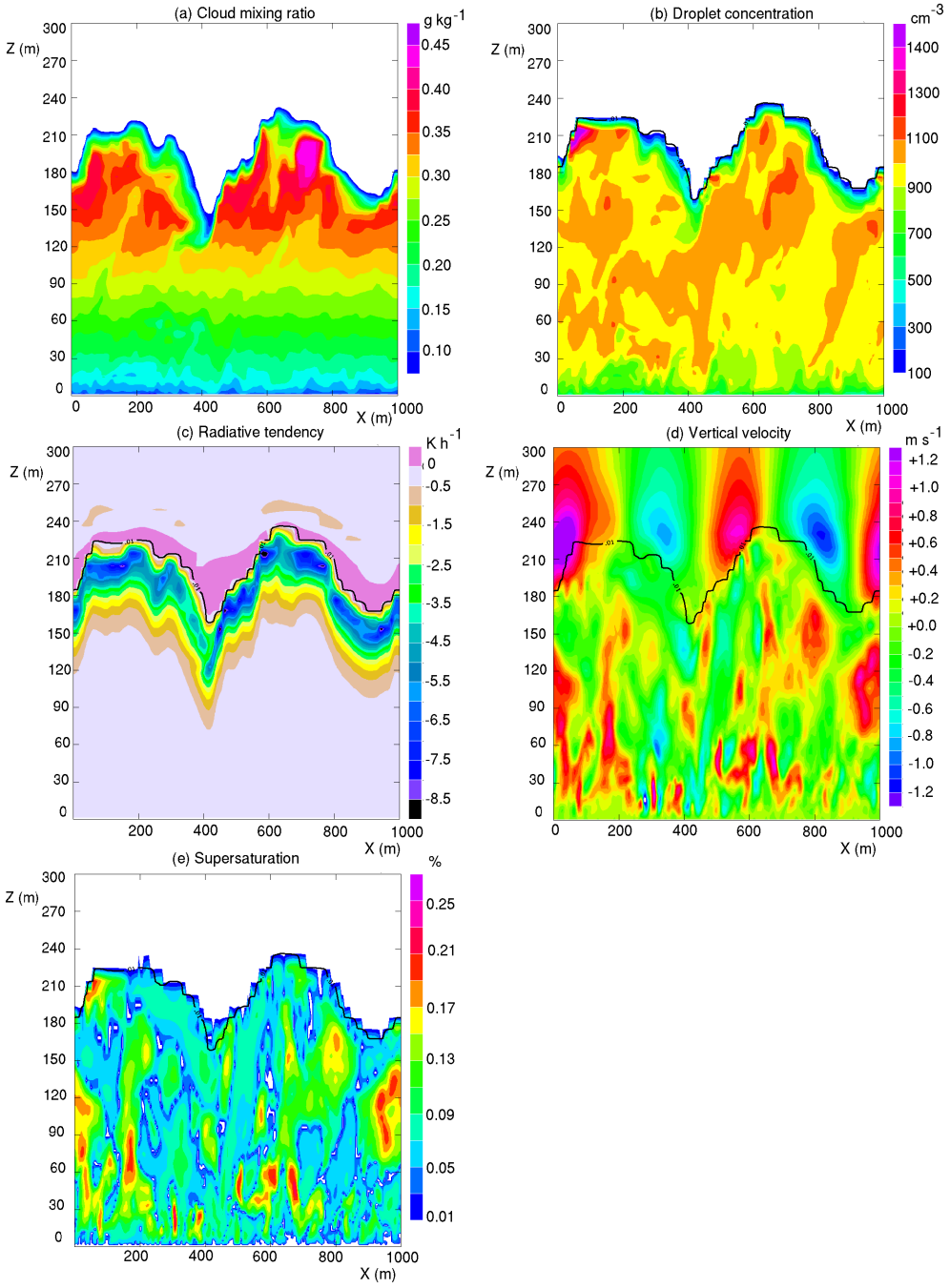

Figure 10. Vertical cross-section at Y=500m at 0620 UTC for the REF simulation: (a) cloud mixing ratio (in $\mathrm{g\,kg^{-1}}$), (b) droplet concentration (in $\mathrm{cm^{-3}}$), (c) radiative tendency (in $\mathrm{K\,h^{-1}}$), (d) vertical velocity (in $\mathrm{m\,s^{-1}}$) and (e) maximum of supersaturation (in $\%$) with the isoline of $r_c = 0.01\ \mathrm{g\,kg^{-1}}$ superimposed.

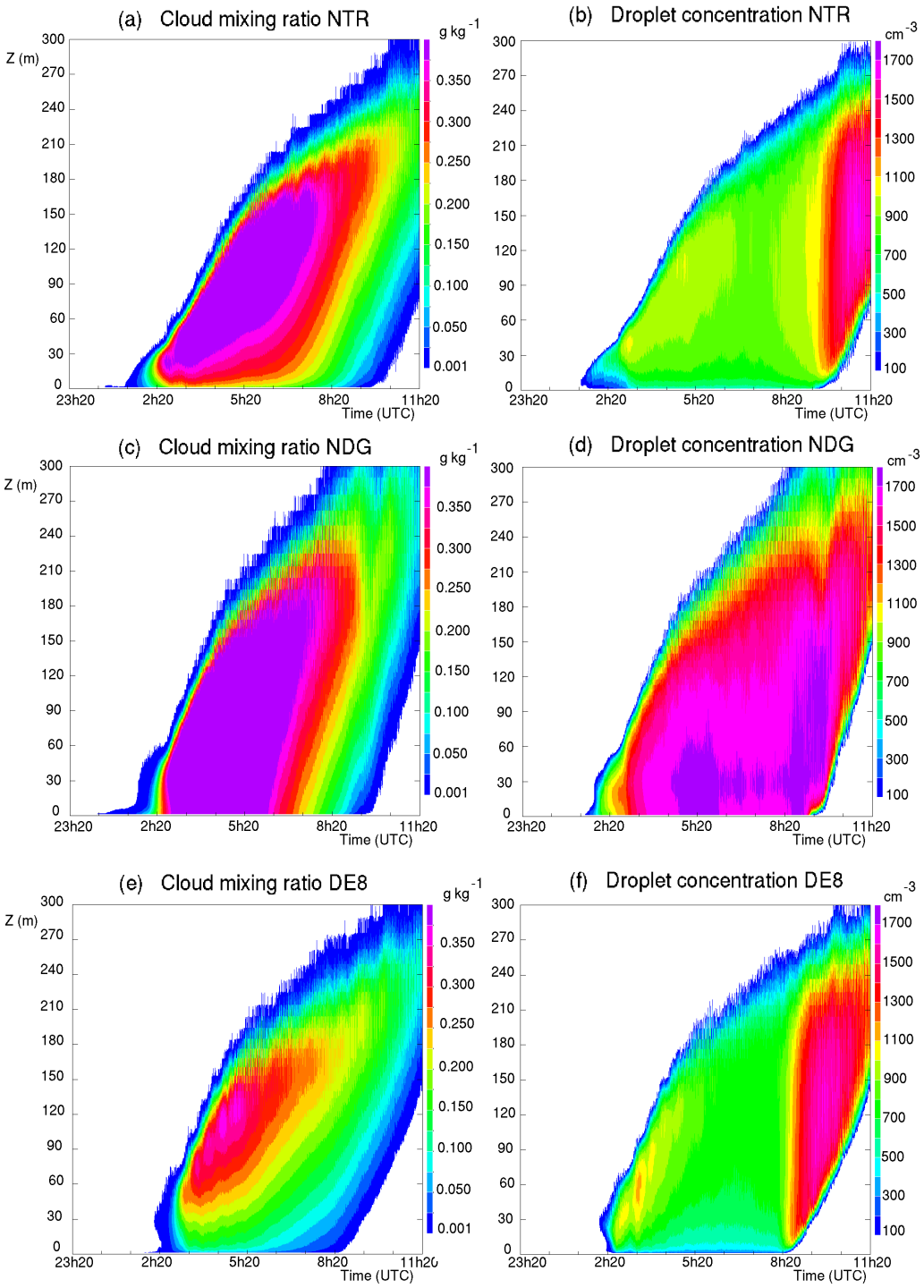

Figure 11. Temporal evolution of simulated vertical profiles of cloud mixing ratio (a, c and e, in $\mathrm{g\,kg^{-1}}$) and droplet concentration (b, d and f, in $\mathrm{cm^{-3}}$) for NTR, NDG and DE8 simulations. Fields are averaged over the horizontal area located downstream of the tree barrier (blue contour area of Fig. 1b).

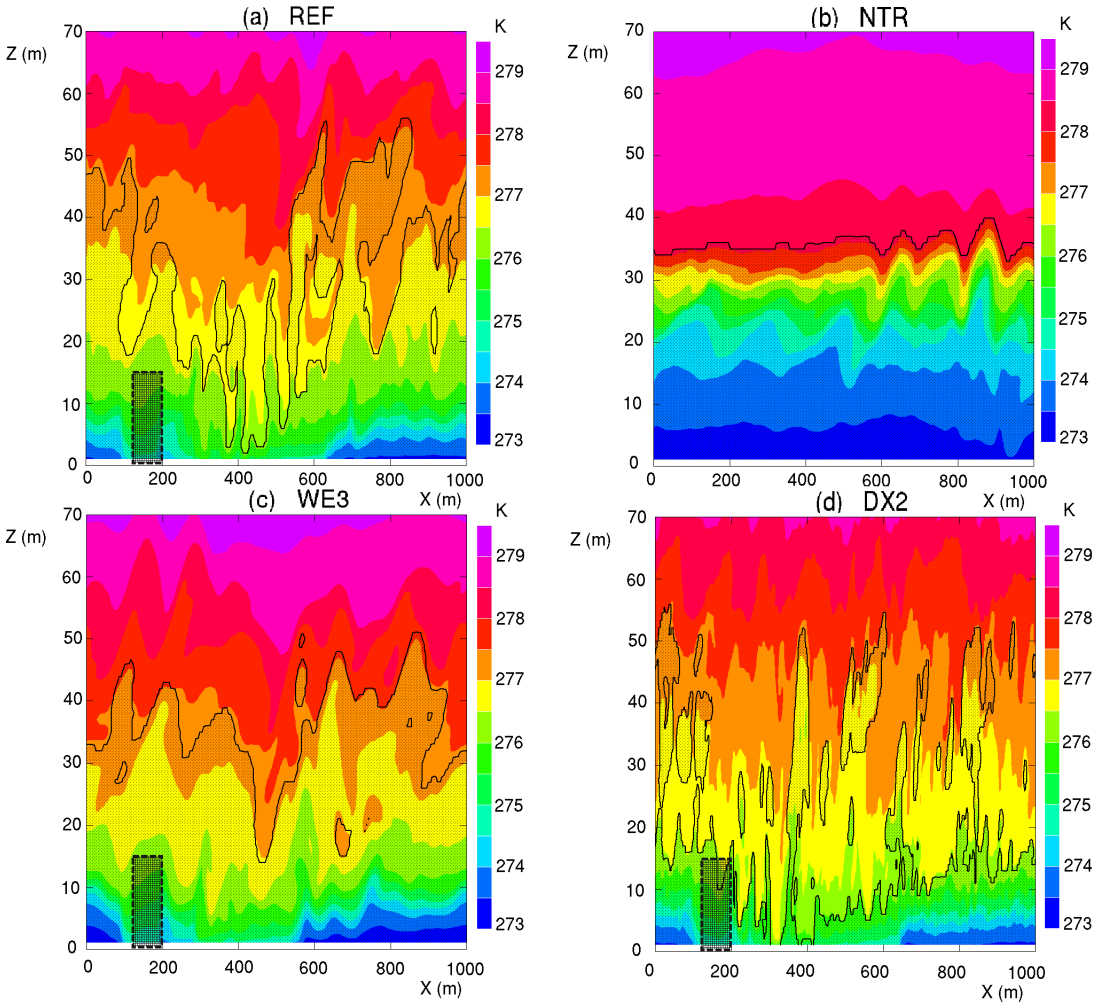

Figure 12. Vertical cross-sections at Y=500m and 0220 UTC of potential temperature (in K) for the REF (a), NTR (b), WE3 (c) and DX2 (d) simulations, with area of cloud mixing ratio higher than $0.1\,\mathrm{g\,kg^{-1}}$ superimposed with dots and the barrier of trees marked with a rectangle..

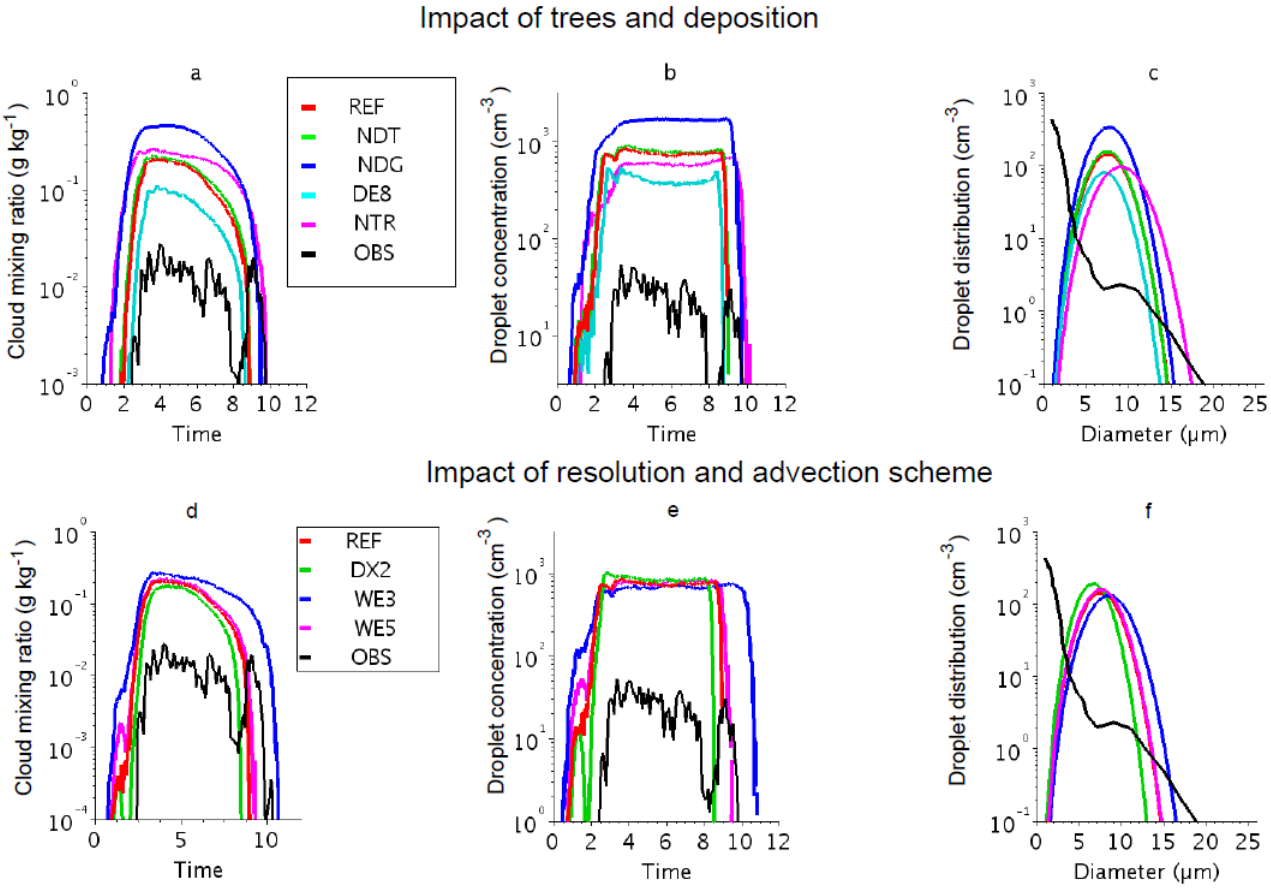

Figure 13. Time series of cloud mixing ratio (a and d, in $\mathrm{g\,kg^{-1}}$), droplet concentration (b and e, in $\mathrm{cm^{-3}}$), and droplet size distribution (c and f, in $\mathrm{cm^{-3}}$) at 0520 UTC and 3 m agl observed (in black), and simulated (in colour). Simulated fields are averaged over the horizontal area located downstream of the tree barrier (blue contour area of Fig. 1b).

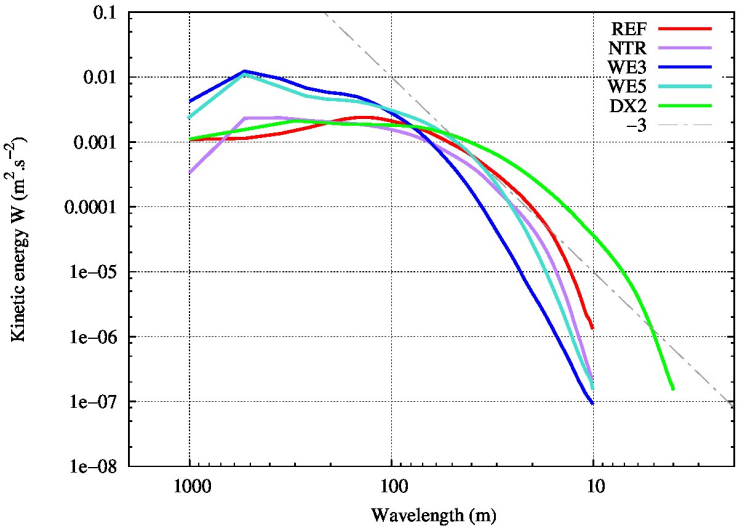

Figure 14. Mean kinetic energy spectra for vertical wind computed over the whole fog layer and horizontal domain at 0620 UTC for the REF, WE3, WE5, DX2 and NTR simulations.

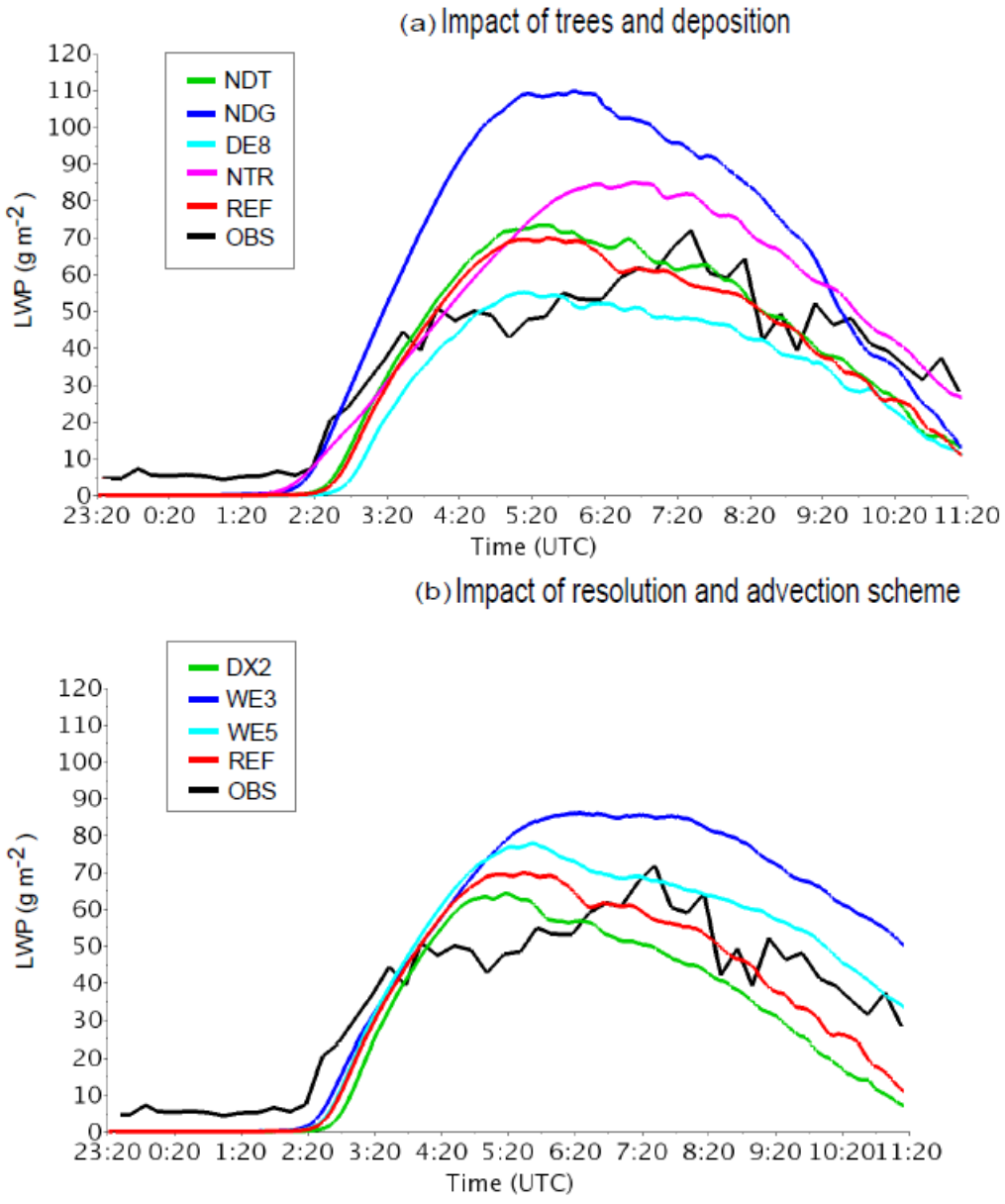

Figure 15. Time series of LWP (in $\mathrm{g\,m^{-2}}$) observed (in black), and simulated (in colour), for the different simulations. Simulated fields are averaged over the horizontal area located downstream of the tree barrier (blue contour area of Fig. 1b).

[A] Appendix: Supporting material

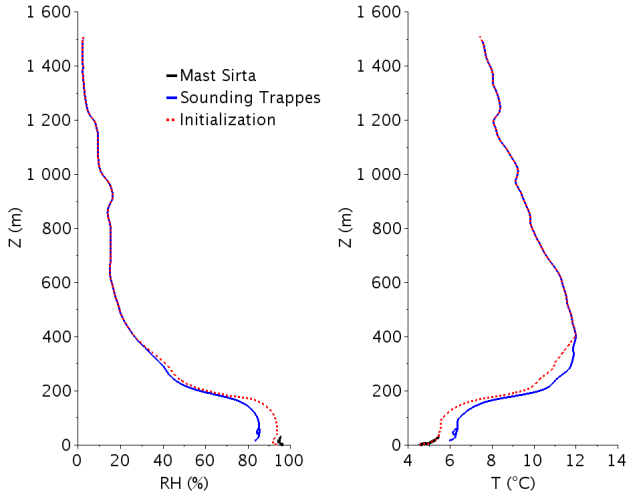

Figure A.1. Relative humidity (in %) and temperature (in C) vertical profiles at 2320 UTC on 14 November 2011 observed at the Sirta mast (in black) and by the Trappes radiosounding (in blue) and used for the REF initialization.

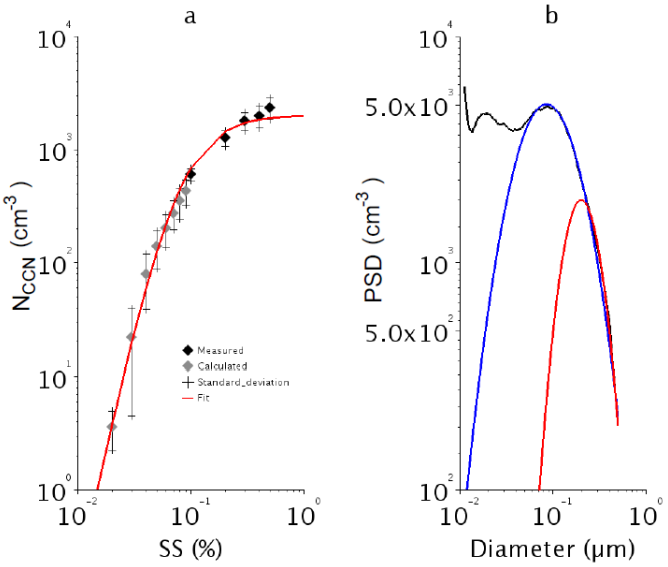

Figure A.2. (a) Activation spectrum: from CCNC measurement before the fog onset (between 0130 and 0230 UTC) for supersaturations higher than 0.1% in black dots, from calculation for supersaturations lower than 0.1% in grey dots, and fitted using Cohard et al.'s (2000c) parametrization in red. (b) Particle size distribution (PSD) from the aerosol measurements (in black), the lognormal distribution fitted on the accumulation mode (in blue) and according to Cohard et al. (2000c) (in red).

References

Aumond, P., V. Masson, C. Lac, B. Gauvreau, S. Dupont, and M. Berengier, 2013: Including the drag effects of canopies: real case large-eddy simulation studies. *Boundary-Layer Meteorology*, **146 (1)**, 65–80.

Baba, Y., and K. Takahashi, 2013: Weighted essentially non-oscillatory scheme for cloud edge problem. *Quarterly Journal of the Royal Meteorological Society*, **139 (674)**, 1374–1388.

Beare, R. J., and M. K. MacVean, 2004: Resolution sensitivity and scaling of large-eddy simulations of the stable boundary layer. *Boundary-Layer Meteorology*, **112 (2)**, 257–281.

Bergot, T., 2013: Small-scale structure of radiation fog: a large-eddy simulation study. *Quarterly Journal of the Royal Meteorological Society*, **139 (673)**, 1099–1112.

Bergot, T., 2015b: Large eddy simulation study of the dissipation of radiation fog. *Quarterly Journal of the Royal Meteorological Society*, **142**, 1029–1040.

Bergot, T., J. Escobar, and V. Masson, 2015a: Effect of small-scale surface heterogeneities and buildings on radiation fog: Large-eddy simulation study at Paris Charles de Gaulle airport. *Quarterly Journal of the Royal Meteorological Society*, **141 (686)**, 285–298.

Bergot, T., E. Terradellas, J. Cuxart, A. Mira, O. Liechti, M. Mueller, and N. W. Nielsen, 2007: Intercomparison of single-column numerical models for the prediction of radiation fog. *Journal of Applied Meteorology and Climatology*, **46 (4)**, 504–521.

Clark, P. A., S. Harcourt, B. Macpherson, C. Mathison, S. Cusack, and M. Naylor, 2008: Prediction of visibility and aerosol within the operational met office unified model. i: Model formulation and variational assimilation. *Quarterly Journal of the Royal Meteorological Society*, **134 (636)**, 1801–1816.

Cohard, J.-M., J.-P. Pinty, and K. Suhre, 2000c: On the parameterization of activation spectra from cloud condensation nuclei microphysical properties. *Journal of Geophysical Research: Atmospheres (1984–2012)*, **105 (D9)**, 11 753–11 766.

Colella, P., and P. R. Woodward, 1984: The piecewise parabolic method (PPM) for gas-dynamical simulations. *Journal of Computational Physics*, **54 (1)**, 174–201.

Cuxart, J., P. Bougeault, and J.-L. Redelsperger, 2000: A turbulence scheme allowing for mesoscale and large-eddy simulations. *Quarterly Journal of the Royal Meteorological Society*, **126 (562)**, 1–30.

Dabas, A., S. Remy, and T. Bergot, 2012: Use of a sodar to improve the forecast of fogs and low clouds on airports. *Pure and Applied Geophysics*, **169 (5-6)**, 769–781.

Deardorff, J. W., 1980: Stratocumulus-capped mixed layers derived from a three-dimensional model. *Boundary-Layer Meteorology*, **18 (4)**, 495–527.

Dupont, J.-C., M. Haeffelin, A. Protat, D. Bouniol, N. Boyouk, and Y. Morille, 2012: Stratus–fog formation and dissipation: a 6-day case study. *Boundary-layer meteorology*, **143 (1)**, 207–225.

Dupont, S., and Y. Brunet, 2008: Edge flow and canopy structure: a large-eddy simulation study. *Boundary-Layer Meteorology*, **126 (1)**, 51–71.

Duynkerke, P. G., 1999: Turbulence, radiation and fog in Dutch stable boundary layers. *Boundary-Layer Meteorology*, **90 (3)**, 447–477.

Fouquart, Y., B. Bonnel, and V. Ramaswamy, 1991: Intercomparing shortwave radiation codes for climate studies. *Journal of Geophysical Research: Atmospheres*, **96 (D5)**, 8955–8968.

Fuzzi, S., and Coauthors, 1998: Overview of the Po valley fog experiment 1994 (CHEMDROP). *Contributions to Atmospheric Physics*, **71 (1)**, 3–19.

Geoffroy, O., J.-L. Brenguier, and I. Sandu, 2008: Relationship between drizzle rate, liquid water path and droplet concentration at the scale of a stratocumulus cloud system. *Atmospheric Chemistry and Physics*, **8 (16)**, 4641–4654.

Guedalia, D., and T. Bergot, 1994: Numerical forecasting of radiation fog. Part ii: A comparison of model simulation with several observed fog events. *Monthly Weather Review*, **122 (6)**, 1231–1246.

Gultepe, I., M. Müller, and Z. Boybeyi, 2006: A new visibility parameterization for warm-fog applications in numerical weather prediction models. *Journal of Applied Meteorology and Climatology*, **45 (11)**, 1469–1480.

Haeffelin, M., and Coauthors, 2010: PARISFOG: shedding new light on fog physical processes. *Bulletin of the American Meteorological Society*, **91 (6)**, 767–783.

Hammer, E., and Coauthors, 2014: Size-dependent particle activation properties in fog during the ParisFog 2012/13 field campaign. *Atmospheric Chemistry and Physics*, **14 (7)**, 10 517–10 533.

Katata, G., 2014: Fogwater deposition modeling for terrestrial ecosystems: A review of developments and measurements. *Journal of Geophysical Research: Atmospheres*, **119 (13)**, 8137–8159.

Khairoutdinov, M., and Y. Kogan, 2000: A new cloud physics parameterization in a large-eddy simulation model of marine stratocumulus. *Monthly Weather Review*, **128 (1)**, 229–243.

Koschmeider, H., 1924: Theorie der horizontalen sichtweite. beifs. *Phys. frei*, 33–53.

Kunkel, B. A., 1984: Parameterization of droplet terminal velocity and extinction coefficient in fog models. *Journal of Climate and Applied Meteorology*, **23 (1)**, 34–41.

Lafore, J., J. Stein, N. Asencio, P. Bougeault, V. Ducrocq, J. Duron, and C. Fischer, 1998: The Meso-NH atmospheric simulation system. Part i: Adiabatic formulation and control simulations. *Annales Geophysicae*, Vol. 16, 90–109.

Langlois, W., 1973: A rapidly convergent procedure for computing large-scale condensation in a dynamical weather model. *Tellus*, **25 (1)**, 86–87.

Lohnert, U., and S. Crewell, 2003: Accuracy of cloud liquid water path from ground-based microwave radiometry 1. dependency on cloud model statistics. *Radio Science*, **38 (3)**.

Lovett, G. M., J. J. Bowser, and E. S. Edgerton, 1997: Atmospheric deposition to watersheds in complex terrain. *Hydrological Processes*, **11 (7)**, 645–654.

Maalick, Z., T. Kuhn, H. Korhonen, H. Kokkola, A. Laaksonen, and S. Romakkaniemi, 2016: Effect of aerosol concentration and absorbing aerosol on the radiation fog life cycle. *Atmospheric Environment*, **133**, 26–33.

Masson, V., and Coauthors, 2013: The SURFEXv7. 2 land and ocean surface platform for coupled or offline simulation of earth surface variables and fluxes. *Geoscientific Model Development*, **6**, 929–960.

Mazoyer, M., F. Burnet, G. C. Roberts, M. Haeffelin, J.-C. Dupont, and T. Elias, 2016: Experimental study of the aerosol impact on fog microphysics. *Atmospheric Chemistry and Physics Discussions*, **2016**, 1–35.

Meyer, M. B., G. G. Lala, and J. E. Jiusto, 1986: Fog-82: A cooperative field study of radiation fog. *Bulletin of the American Meteorological Society*, **67 (7)**, 825–832.

Mlawer, E. J., S. J. Taubman, P. D. Brown, M. J. Iacono, and S. A. Clough, 1997: Radiative transfer for inhomogeneous atmospheres: RRTM, a validated correlated-k model for the longwave. *Journal of Geophysical Research: Atmospheres (1984–2012)*, **102 (D14)**, 16 663–16 682.

Morcrette, J.-J., 1991: Radiation and cloud radiative properties in the European Centre for Medium Range Weather Forecasts forecasting system. *Journal of Geophysical Research: Atmospheres*, **96 (D5)**, 9121–9132.

Nakanishi, M., 2000: Large-eddy simulation of radiation fog. *Boundary-Layer Meteorology*, **94 (3)**, 461–493.

Noilhan, J., and S. Planton, 1989: A simple parameterization of land surface processes for meteorological models. *Monthly Weather Review*, **117 (3)**, 536–549.

Porson, A., J. Price, A. Lock, and P. Clark, 2011: Radiation fog. Part ii: Large-eddy simulations in very stable conditions. *Boundary-Layer Meteorology*, **139 (2)**, 193–224.

Price, J., 2011: Radiation fog. Part i: observations of stability and drop size distributions. *Boundary-Layer Meteorology*, **139 (2)**, 167–191.

Price, J., and R. Clark, 2014: On the measurement of dewfall and fog-droplet deposition. *Boundary-Layer Meteorology*, **152 (3)**, 367–393.

Pruppacher, H. R., J. D. Klett, and P. K. Wang, 1998: Microphysics of clouds and precipitation.

Ricard, D., C. Lac, S. Riette, R. Legrand, and A. Mary, 2013: Kinetic energy spectra characteristics of two convection-permitting limited-area models AROME and Meso-NH. *Quarterly Journal of the Royal Meteorological Society*, **139 (674)**, 1327–1341.

Roach, W., R. Brown, S. Caughey, J. Garland, and C. Readings, 1976: The physics of radiation fog: I–a field study. *Quarterly Journal of the Royal Meteorological Society*, **102 (432)**, 313–333.

Roberts, G., and A. Nenes, 2005: A continuous-flow streamwise thermal-gradient ccn chamber for atmospheric measurements. *Aerosol Science and Technology*, **39 (3)**, 206–221.

Savijärvi, H., A. Arola, and P. Räisänen, 1997: Short-wave optical properties of precipitating water clouds. *Quarterly Journal of the Royal Meteorological Society*, **123 (540)**, 883–899.

Seity, Y., P. Brousseau, S. Malardel, G. Hello, P. Bénard, F. Bouttier, C. Lac, and V. Masson, 2011: The AROME-France convective-scale operational model. *Monthly Weather Review*, **139 (3)**, 976–991.

Shu, C.-W., 1998: Essentially non-oscillatory and weighted essentially non-oscillatory schemes for hyperbolic conservation laws. *Advanced numerical approximation of nonlinear hyperbolic equations*, Springer, 325–432.

Skamarock, W. C., 2004: Evaluating mesoscale nwp models using kinetic energy spectra. *Monthly Weather Review*, **132 (12)**, 3019–3032.

Slingo, A., 1989: A GCM parameterization for the shortwave radiative properties of water clouds. *Journal of the Atmospheric Sciences*, **46 (10)**, 1419–1427.

Stolaki, S., M. Haeffelin, C. Lac, J.-C. Dupont, T. Elias, and V. Masson, 2015: Influence of aerosols on the life cycle of a radiation fog event. A numerical and observational study. *Atmospheric Research*, **151**, 146–161.

Tardif, R., 2007: The impact of vertical resolution in the explicit numerical forecasting of radiation fog: A case study. *Pure and Applied Geophysics*, **164 (6-7)**, 1221–1240.

Thouron, O., J.-L. Brenguier, and F. Burnet, 2012: Supersaturation calculation in large eddy simulation models for prediction of the droplet number concentration. *Geoscientific Model Development*, **5 (3)**, 761–772.

Uematsu, A., M. K. Yamamoto, H. Hashiguchi, K. Hirashima, and S. Fukao, 2005: Shear-induced roll structure of fog observed by a millimeter-wave scanning Doppler radar. *Geophysical Research Letters*, **32 (14)**.

von Glasow, R., and A. Bott, 1999: Interaction of radiation fog with tall vegetation. *Atmospheric Environment*, **33 (9)**, 1333–1346.

Wendisch, M., and Coauthors, 1998: Drop size distribution and LWC in Po valley fog. *Contributions to Atmospheric Physics*, **71 (1)**, 87–100.

Ye, X., B. Wu, and H. Zhang, 2015: The turbulent structure and transport in fog layers observed over the Tianjin area. *Atmospheric Research*, **153**, 217–234.

Zaïdi, H., E. Dupont, M. Milliez, L. Musson-Genon, and B. Carissimo, 2013: Numerical simulations of the microscale heterogeneities of turbulence observed on a complex site. *Boundary-Layer Meteorology*, **147 (2)**, 237–259.

Zhang, J., H. Xue, Z. Deng, N. Ma, C. Zhao, and Q. Zhang, 2014a: A comparison of the parameterization schemes of fog visibility using the in-situ measurements in the North China Plain. *Atmospheric Environment*, **92**, 44–50.

Zhang, X., L. Musson-Genon, E. Dupont, M. Milliez, and B. Carissimo, 2014b: On the influence of a simple microphysics parametrization on radiation fog modelling: A case study during ParisFog. *Boundary-Layer Meteorology*, **151 (2)**, 293–315.